DESIGN FABRICATION AND CHARACTERIZATION OF HIGH PERFORMANCE RESONANT CAVITY ENHANCED PHOTODETECTORS

A THESIS
SUBMITTED TO THE DEPARTMENT OF ELECTRICAL AND
ELECTRONICS ENGINEERING
AND THE INSTITUTE OF ENGINEERING AND SCIENCE
OF BILKENT UNIVERSITY
IN PARTIAL FULFILLMENT OF THE REQUIREMENTS
FOR THE DEGREE OF
MASTER OF SCIENCE

By
Necmi Bıyıklı
September 1998

DESIGN, FABRICATION AND CHARACTERIZATION OF HIGH PERFORMANCE RESONANT CAVITY ENHANCED PHOTODETECTORS

A THESIS

SUBMITTED TO THE DEPARTMENT OF ELECTRICAL AND ELECTRONICS

ENGINEERING

AND THE INSTITUTE OF ENGINEERING AND SCIENCE

OF BILKENT UNIVERSITY

IN PARTIAL FULFILLMENT OF THE REQUIREMENTS

FOR THE DEGREE OF

MASTER OF SCIENCE

By

Necmi Bıyıklı

September 1998

I certify that I have read this thesis and that in my opinion it is fully adequate, in scope and in quality, as a dissertation for the degree of Master of Science.
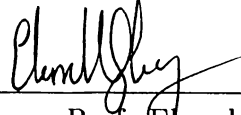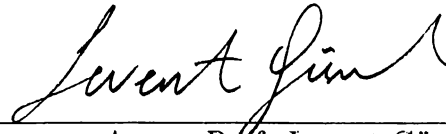
Assoc. Prof. Orhan Aytür (Supervisor)

I certify that I have read this thesis and that in my opinion it is fully adequate, in scope and in quality, as a dissertation for the degree of Master of Science.

Assoc. Prof. Ekmel Özbay

I certify that I have read this thesis and that in my opinion it is fully adequate, in scope and in quality, as a dissertation for the degree of Master of Science.

Assoc. Prof. Levent Gürel

Approved for the Institute of Engineering and Science:

Prof. Mehmet Baray,
Director of Institute of Engineering and Science

Abstract

DESIGN, FABRICATION AND CHARACTERIZATION OF HIGH PERFORMANCE RESONANT CAVITY ENHANCED PHOTODETECTORS

Necmi Bıyıklı

M. S. in Electrical and Electronics Engineering

Supervisor: Assoc. Prof. Orhan Aytür

September 1998

Photodetectors are essential components of optoelectronic integrated circuits and fiber optic communication systems. For higher system performances, photoreceivers with high bandwidth-efficiency products are needed. A new family of photodetectors introduced in the early 90's offers high performance detection along with wavelength selectivity: resonant cavity enhanced (RCE) photodetectors. In this thesis, we present our efforts for the design, fabrication and characterization of AlGaAs/GaAs-based Schottky and p-i-n type RCE photodiodes operating within the first optical communication window. Epitaxial wafers are designed using scattering matrix method based simulations and grown with molecular beam epitaxy. Schottky photodiode was primarily designed for high-speed operation, where as in p-i-n structure we aimed to achieve near unity quantum efficiency. Measurement results show reasonable agreement with our theoretical simulations. Fabricated Schottky and p-i-n RCE photodiode samples demonstrated high bandwidth-efficiency products, 36 and 46 GHz respectively. These results indicate the best performances for RCE Schottky and p-i-n photodiodes reported in scientific literature.

Özet

YÜKSEK PERFORMANSLI, RESONANT KAVİTE KATKILI FOTODETEKTÖRLERİN TASARIMI, ÜRETİMİ VE KARAKTERİZASYONU

Necmi Bıyıklı

Elektrik ve Elektronik Mühendisliği Yüksek Lisans

Tez Yöneticisi: Doç. Dr. Orhan Aytür

Eylül 1998

Fotodetektörler optoelektronik entegre devrelerin ve fiber optik haberleşme sistemlerinin önemli elemanlarındandır. Daha yüksek sistem performansi icin yüksek hız-verim çarpımına sahip fotodetektörlere ihtiyaç var. 90'lı yılların başında geliştirilen yeni bir fotodetektör tipi yüksek performansın yanısıra dalgaboyu seçiciliği vaadediyordu: resonant kavite katkılı (RCE) fotodetektörler. Bu tezde, birinci optik haberleşme penceresinde calisan, AlGaAs/GaAs temelli Schottky ve p-i-n RCE fotodiyotlarin tasarımı, üretimi ve karakterizasyonu için yaptığımız çalışmaları sunuyoruz. Diyot yapılarının tasarımı dağılmış parametreli matris metoduna dayalı simülasyonlar ile gerçekleştirilirken, yapılar moleküler ışın büyütümü tekniğiyle büyütüldü. Schottky fotodiyot öncelikle yüksek hızlı performans hedeflenerek tasarlandı. Buna karşılık p-i-n tasarımında asıl hedef 100%'e yakın verim elde etmekti. Ölçüm sonuçları teorik simülasyonlarla kabul edilebilir bir uygunluk gösterdi. Üretilen Schottky ve p-i-n RCE fotodiyot örneklerinde yüksek hız-verim çarpımlarına (sırasıyla 36 GHz ve 46 GHz) ulaştik. Elde ettiğimiz bu rakamlar akademik literatürde RCE Schottky ve p-i-n fotodiyotlari alanında ulaşılan en iyi performanslara karşılık gelmektedir.

Anahtar

sözcükler: Fotodetektör, Fotodiyot, Schottky Fotodiyot, P-İ-N Fotodiyot, Resonant Kavite, Resonant Kavite Katkılı, Kuantum Verimi, Yüksek Hız, Yüksek Hız-Verim Çarpımı.

Acknowledgement

i

Contents

List of Figures

Chapter 1

Introduction

'This telephone has too many shortcomings to be seriously considered as a means of communication. The device is inherently of no value to us.' (Western Union internal memo, 1876)

How could they know at that time that the invention of the telephone by Alexander Graham Bell will lead to an enormous world wide telecommunication market, which earns 1.5 trillion USD each year? The invention of the solid-state transistor in 1947, opened the age of computing and communications. In 1960s, researchers developed the first operational laser. The development of the first commercially feasible optical fiber in 1970s made the fiber optic communications a promising candidate for telecommunications. Demand for faster, cheaper and less noisy communications has replaced the copper wire with the optical fiber. Semiconductor lasers and photodetectors are developed and used as transmitters and receivers in these systems. With the developing photonics technology, the cost for a transatlantic phone call has decreased by three orders of magnitude since 1956.

Hence, telecommunications was, and still is, the main driving source for the rapidly growing optoelectronics industry. Lasers, modulators, photodetectors, optical amplifiers, and optical fiber are the main components of an optical communication system. The optical fiber offers an operation bandwidth up to tens of THz. The research effort going on in optoelectronics is mainly

1

devoted to fully exploit the fiber bandwidth. This will be possible with high performance components, including photodetectors. High-speed and high-efficiency photodetectors are vital components of optoelectronic systems,[1] including fiber optic communications.

Semiconductor based photodiodes demonstrate excellent features to fulfill the requirements of a high-speed optoelectronic receiver. Several semiconductor material systems are successfully employed for high-speed photodetection. GaAs is one of the most widely studied semiconductor for photodetection. GaAs based Schottky and p-i-n photodiodes have demonstrated bandwidth capabilities as high as 200 GHz.[2-7] Furthermore, using low temperature grown GaAs, photodetectors with bandwidths up to 550 GHz have also been demonstrated.[8,9] However, the efficiency of these detectors have been typically limited to less than 10%, mostly due to the thin absorption region needed for short transit times. One can increase the absorption region thickness to achieve higher efficiencies. But this also means longer transit times that will degrade the high-speed performance of the devices. This trade-off limits the bandwidth-efficiency product, i.e. the overall performance of the photodiodes.

Resonant cavity enhanced (RCE) photodetectors potentially offer the possibility of overcoming this limitation of the bandwidth-efficiency product of conventional photodetectors.[10,11] The RCE detectors are based on the enhancement of the optical field within a Fabry-Perot resonant microcavity. The increased field allows the usage of thin absorbing layers, which minimizes the transit time of the photogenerated carriers without sacrificing the quantum efficiency. It also introduces wavelength selectivity which is a desired feature for wavelength division multiplexing (WDM) applications[12-14] in optical communications.

RCE photodetection research has mainly concentrated on three different type of detectors: Schottky, p-i-n and avalanche photodiodes. Best performances reported for RCE Schottky photodiodes are 100 GHz bandwidth[15] and a bandwidth-efficiency product over 25 GHz.[16] RCE p-i-n photodiode is the most widely investigated type of photodiode in RCE literature. Although theoretical studies show that over 100 GHz bandwidth-efficiency products should

be achievable with RCE heterojunction p-i-n designs,[17-19] the best results extend to 17 GHz bandwidth-efficiency product.[20] A 33 GHz maximum bandwidth is reported for an RCE avalanche photodiode operating in the low-gain regime.[21]

Hence, we are still far away from the THz regime in optical communication systems as far as detector performances are concerned. Demand for higher performance photodetectors is the main motivation of this thesis work. We aimed to contribute to the detector peroformance using the RCE photodetection scheme. We applied this technique to GaAs-based Schottky and p-i-n photodiode structures, operating within the 800-850 nm wavelength regime. Measurements of the fabricated devices have shown high bandwidth-efficiency products.

Chapter 2 reviews the operation principles and characteristics of photodiodes. RCE theory is introduced as a solution for the bandwidth-efficiency trade-off. Design criteria and optimization parameters are presented at the end of the chapter. Chapter 3 is devoted to the design of RCE photodiode. After a brief review about the material systems for RCE photodetection, device simulation technique (scattering metrix method) is described. Then the epitaxial structure of Schottky and p-i-n designs are introduced with their spectral reflectivity measurements. Fabrication process of RCE photodiodes is explained in Chapter 4, along with the I-V characterization of the fabricated devices. Quantum efficiency and bandwidth measurement results are reported in Chapter 5, followed by future directions and plans in high performance photodetector area.

Chapter 2

Theoretical Background

Photodetectors can be classified into two basic categories: Thermal detectors and quantum detectors.[22] Thermal detectors sense the radiation by its heating effect. Bolometers, thermistors, pyroelectric detectors are widely used thermal detectors that can operate in a very broad spectral range. However, their bandwidth and sensitivity performances are relatively poor. The operation principle of quantum photodetectors is based on the quantum (discrete) nature of photons. These detectors have the capability of transferring the photon energy to individual particles (electrons) so that a proportional photocurrent or photovoltage is created. Photoemissive, photoconductive and photovoltaic detectors fall within this category of photodetectors. They have limited spectral response, but demonstrate high sensitivity and high speed which are essential characteristics for optical communication systems. Photoconductive and photovoltaic detectors are semiconductor based photodetectors. Photoconductive detectors detect the radiation by sensing the change of conductivity of the material. The conductivity change of the material is proportional to the radiation intensity falling on the semiconductor material. The ability to form rectifying junctions is the basis of photovoltaic detectors, also known as photodiodes. Under illumination, the excess carriers created within the semiconductor generate a proportional output current. Since our work is on photodiodes, operating principles of a photodiode is given in detail in the following sections. The operation differences between

4

Schottky and p-i-n photodiodes will also be discussed. At the end of the chapter, resonant cavity enhancement (RCE) effect will be introduced as a solution to the bandwidth-efficiency trade-off in photodiodes.

2.1   Photodiode Operation

Basically, photodiode operation is the transportation of the photogenerated carriers through the diode junction. When light is incident on the rectifying junction (p-n or metal-semiconductor), photons having enough energy ($hv > E_g$) are absorbed. The excess electrons and holes created are separated by the built-in junction field and collected at different sides of the diode. If the diode is connected through an external load, a current is developed which is proportional to the number of photons absorbed and the carriers generated.

Photodiodes include p-n junction diodes, Schottky diodes, p-i-n diodes and heterojunction diodes, according to the junction types forming the diode. The photodetection mechanisms and carrier dynamics of Schottky and p-i-n photodiodes will be analyzed in the following paragraphs.

2.1.1   Schottky Photodiode

A Schottky diode consists of a metal-semiconductor junction. The energy band-diagram of a Schottky junction is shown in Figure 2.1, where the Fermi level
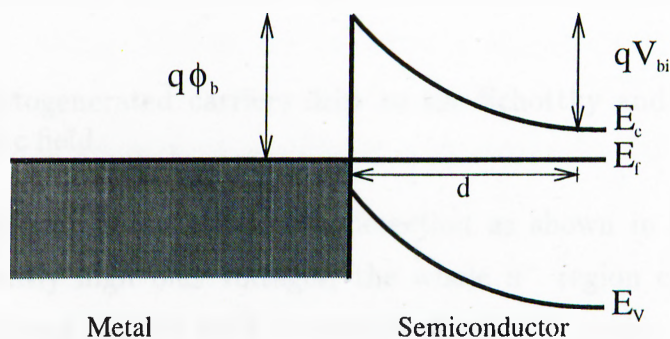
Figure 2.1: Energy band-diagram of a Schottky junction.

pinning at the interface can be seen. The difference between the work functions (difference between vacuum level and Fermi level) of metal and semiconductor is defined as the contact potential, $q\phi_b$, and acts as a potential barrier for the charged carriers. This potential barrier forms a depletion region with a total voltage drop of V_{bi} (built-in potential) across this region. The resulting device is a Schottky diode, which acts as a voltage rectifier.[23] Schottky photodiodes are excellent for detection of UV and visible radiation and are the fastest semiconductor photodetectors available. However, these diodes show poor efficiency performance, due to thin absorption regions and the highly absorbing metal layer.
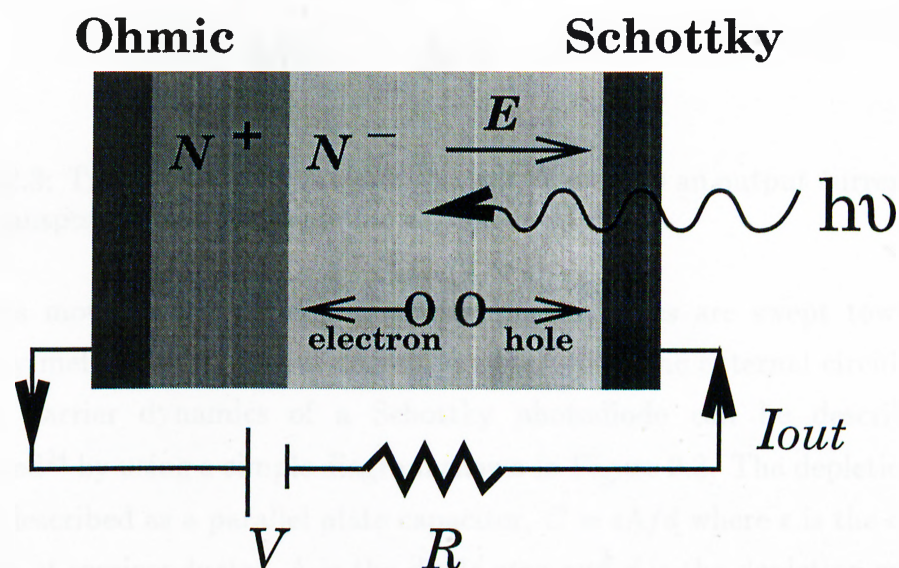
Figure 2.2: Photogenerated carriers drift to the Schottky and ohmic contacts under the electric field.

Such a diode can be used for photodetection as shown in Figure 2.2. By applying sufficiently high bias voltages, the whole n^- region can be depleted, so that a continuous electric field is created across this region. Photons with sufficient energies are absorbed in the depletion region and electron-hole pairs are generated. The generated carriers are swept away by the electric field. While
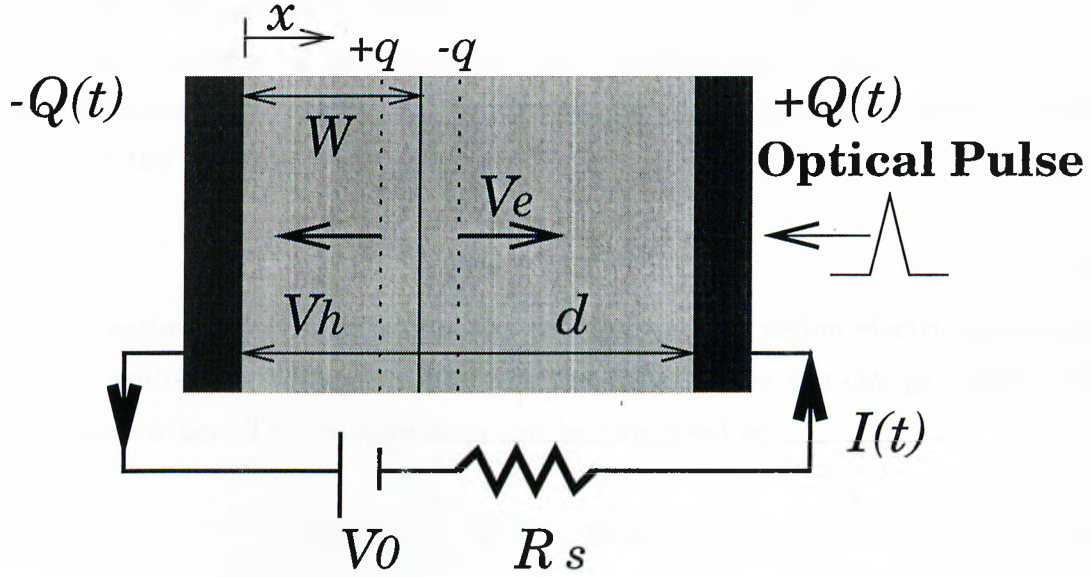
Figure 2.3: The carriers generated at a depth W induces an output current during their transport across the depletion region.

electrons move to the n^+ doped semiconductor, holes are swept towards the Schottky metal and an output current is observed at the external circuit.

The carrier dynamics of a Schottky photodiode can be described and calculated[24] by using a simple diagram shown in Figure 2.3. The depletion region can be described as a parallel plate capacitor, $C = \epsilon A/d$ where ϵ is the dielectric constant of semiconductor, A is the diode area and d is the depletion width. At steady state, the voltage bias on the capacitor is V_0, which results in a steady state total charge of $Q_0 = CV_0$ across the capacitor.

The position dependent electric field across the depletion region, $E(x)$ has the following relation with the bias voltage:

$$V_0 = \int_0^d E(x)dx \qquad (2.1)$$

Let's assume that, at $t = 0$, a narrow optical pulse generates carriers with a total charge of q, at a depth W from the Schottky surface. This will generate traveling

positive and negative sheet charges with sheet charge densities ρ and $-\rho$, where $\rho = q/A$. The positively charged sheet corresponds to the holes moving at the hole drift velocity, v_h and the negatively charged sheet denotes the electrons with electron drift velocity, v_e. As a result, an additional electric field is formed between the sheets.

$$E_\sigma = \frac{\sigma}{\epsilon} = \frac{q}{A\epsilon} \tag{2.2}$$

The direction of this field is opposite to the depletion region electric field $E(x)$, which results in a voltage drop across the capacitor as the charge moves away from each other. This voltage drop can be expressed as

$$V_\sigma(t) = \int_{x_h}^{x_e} E\sigma dx = E\sigma[x_e(t) - x_h(t)] \tag{2.3}$$

where $x_e t$ and $x_h t$ are the time dependent coordinates of the negative and positively charged sheets. These time dependent coordinates can be expressed as,

$$x_e(t) = W + v_e t \qquad \text{for } 0 < t < t_e \tag{2.4}$$

$$x_h(t) = W - v_h t \qquad \text{for } 0 < t < t_h \tag{2.5}$$

where the electron transit time, $t_e = (d-W)/v_e$, and hole transit time, $t_h = W/v_h$ are defined as time durations required for each carrier to complete its transport. Assuming $t_h > t_e$ and using Equation 2.18 we can express the time dependent voltage drop as,

$$V_\sigma(t) = \begin{cases} \frac{q}{A\epsilon}(v_e + v_h)t & \text{for } 0 < t < t_e \\ \frac{q}{A\epsilon} v_h t & \text{for } t_e < t < t_h \end{cases} \tag{2.6}$$

Inserting this equation into the following two equations,

$$I_{out}(t) = \frac{dQ(t)}{dt} = \frac{d}{dt}[CV(t)] \tag{2.7}$$

$$V(t) = V_0 - V_\sigma(t) \tag{2.8}$$

The induced output current, I_{out} can be written as

$$I_{out}(t) = \begin{cases} I_1 = \frac{q}{d}(v_e + v_h) & \text{for } 0 < t < t_e \\ I_2 = \frac{q}{d}v_h & \text{for } t_e < t < t_h \end{cases} \tag{2.9}$$

and is shown in Figure 2.4.
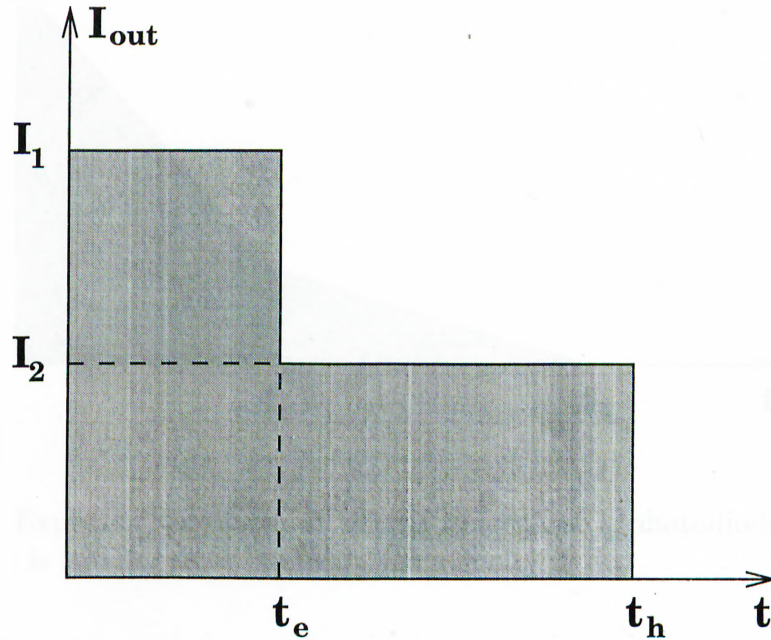
Figure 2.4: Time-dependence waveform of the induced current.

The total charge under the curve equals to q, confirming the charge conservation of the system. An amount of charge generates a current such that the same amount of charge accumulates on the capacitor. Once all the carriers reach to the parallel plates, they recombine with these excess charge and steady state is reached.

The analysis above was for a charge generation at $x = W$. If we integrate over entire depletion region, d, we obtain the output current waveform as shown in Figure 2.5. Here $v_e > v_h$ is assumed, which is the case for most of semiconductors. Also a uniform density of photogenerated carriers, e.g. constant

optical power across the depletion region is assumed, which is a valid assumption for semiconductors with small absorption coefficients.
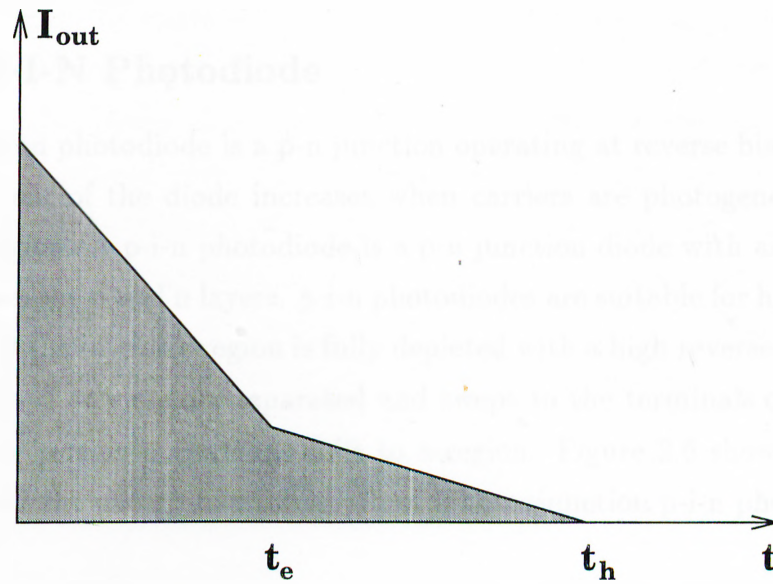
Figure 2.5: Expected waveform of output current of a photodiode where hole drift velocity is smaller than electron drift velocity.

The output current is proportional to the number of carriers that continue their transport. At $t = 0$, the number of carriers that induce the output current is maximum, so that I_{out} displays its maximum at that time. But as the carriers closest to the metal and the other end of the depletion region complete their transport, the number of carriers continuing their transport decreases at a linear rate. At $t = t_e$, the last electrons drifting from $x = 0$ to $x = d$ have completed their travel, while there are still traveling holes. Holes generated at $x = d$ complete their transport the latest, at $t = d/v_h$. The slowering effect of holes is seen as a tail in the output current waveform. This is a major problem of photodiodes as high-speed operation is concerned. One can get rid of this problem by using heterostructures, i.e. using different materials for absorption region and intermediate regions. All layers but the absorption layer will be transparent for the spectrum of interest, so that all electron-hole pairs are generated only in this

region. By adjusting the placement of the active region, the response time of the diode can be minimized by equalizing the hole transit time to the electron transit time, so that no tail is observed at the output waveform.

2.1.2   P-I-N Photodiode

A p-n junction photodiode is a p-n junction operating at reverse bias mode. The reverse current of the diode increases when carriers are photogenerated in the depletion region. A p-i-n photodiode is a p-n junction diode with an intrinsic (i) layer between the p and n layers. p-i-n photodiodes are suitable for high-efficiency operation. If the intrinsic region is fully depleted with a high reverse bias voltage, photogenerated carriers are separated and swept to the terminals of the device: holes drift to p-region, electrons drift to n-region. Figure 2.6 shows the typical structure and the energy-band diagram of a homojunction p-i-n photodiode.[25]
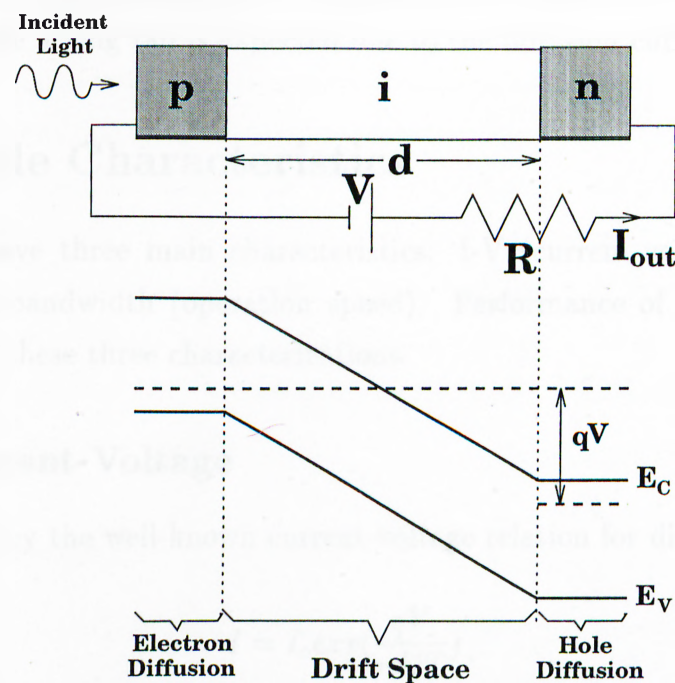
Figure 2.6: Photodiode structure and energy band-diagram of a homojunction p-i-n photodiode.

Classical (homojunction) p-i-n photodiodes lack from high-speed operation since there is a diffusion component in the output current. The carriers which are photogenerated within the p and n layers can only contribute to the photocurrent by diffusing into the intrinsic layer. Once they reach the i layer, they are swept by the high electric field. Since these carriers are diffusing instead of drifting within the doped layers, these diodes demonstrate much slower operation speeds than Schottky photodiodes. To overcome this handicap, heterojunction p-i-n photodiodes can be utilized, where p and n layers have a wider bandgap than i layer so that no photogeneration occurs in these layers. So there is no diffusion current contributing to the output current. Hence with heterojunction p-i-n photodiodes high efficiency can be achieved with high operation speeds.

The carrier transportation mechanism in a p-i-n photodiode is very similar to the Schottky photodiode. Instead of a metal, there is a p^+ doped layer. The current-voltage characteristics are also very similar. Similar I_{out} waveforms are expected from a heterojunction p-i-n photodiode, whereas for a homojunction p-i-n photodiode a long tail is expected due to the diffusion current.

2.2 Diode Characteristics

Photodiodes have three main characteristics: I-V (current-voltage), quantum efficiency, and bandwidth (operation speed). Performance of a photodiode is measured with these three characterizations.

2.2.1 Current-Voltage

Photodiodes obey the well-known current-voltage relation for diodes,

$$I = I_o exp(\frac{qV}{nKT}) \tag{2.10}$$

Low dark current and high breakdown voltage are two indicators of diode junction quality. Low dark current means higher sensitivity. It is the current flowing through the diode under reverse bias and without illumination. The photodiode

operates in the avalanche breakdown region when sufficiently high reverse bias is applied. This reverse bias voltage value corresponds to the breakdown voltage and determines the limit of reverse bias voltage that can be applied for photodiode operation. After this value, gain and multiplication mechanisms begin to effect the diode operation.[25]

2.2.2 Quantum Efficiency

Quantum efficiency of a photodiode, η, is defined as the probability that a single photon incident on the photodiode will create an electron-hole pair that contributes to the output current, i.e. it is the ratio of the number of detected electrons to the number of incident photons. For classical photodiodes the expression for quantum efficiency is

$$\eta = (1 - R)(1 - e^{-\alpha d}) \tag{2.11}$$

where R is the front surface reflectivity, α is the power absorption coefficient and d is the thickness of the absorbing semiconductor layer. The first term represents the transmitted optical power and the second term denotes the portion of optical power absorbed during the single pass through the absorbing layer. So to maximize the quantum efficiency, one should minimize the detector surface reflectivity, R and maximize the single pass absorption, αd. R can be minimized for a specific spectral range using anti-reflection coatings. Single pass absorption can be simply increased by increasing d. So, it is not a difficult task to achieve near-unity quantum efficiencies.

2.2.3 Bandwidth

Another important device characteristic is the operation speed (bandwidth) of the photodiode. As discussed previously, the response time is mainly limited by the transit times of the photogenerated carriers. The other factors are the RC time constant of the photodiode circuit and diffusion of carriers generated in the undepleted regions. Schottky and heterojunction photodiode designs solve

the carrier diffusion problem. Transit times can be reduced by decreasing the depletion region width, d. However if d is decreased, the capacitance increases and RC time constant becomes the main bandwidth limitation. The transit time and capacitance limited 3 dB bandwidths are respectively expressed as

$$f_{tr} = 0.45\frac{v}{d} \tag{2.12}$$

$$f_{RC} = \frac{d}{2\pi R\epsilon A} \tag{2.13}$$

where d is the depletion width, v is the carrier drift velocity, R is the total resistance, A is the device area and ϵ is the permittivity of the semiconductor. For a given A and R, there exists an optimum d value. By reducing the active layer thickness one should be able to achieve high bandwidths as long as the capacitance is concurrently decreased by reducing the device size. So assuming no capacitance limitation, bandwidth of the photodetector is inversely proportional to d.

2.2.4 Bandwidth-Efficiency Trade-off

It is desirable to achieve both high speed and high quantum efficiency with a single photodetector. However as discussed above, bandwidth and efficiency have inverse dependencies on active layer thickness, d. Near unity quantum efficiencies and very large bandwidths can be realized with very thick and very thin absorption layers respectively. But for any d, bandwidth-efficiency product remains almost constant. The bandwidth-efficiency product of a photodetector determines its overall performance. To combine high efficiency and high bandwidth, one needs to increase this product. Resonant cavity enhancement (RCE) effect offers a clever solution to increase the bandwidth-efficiency product of a photodiode.

2.3 Resonant Cavity Enhancement

This effect is first proposed by Unlu *et. al.* in 1990[26] and is applied to a broad range of photodetector types: Schottky,[27,28] p-i-n[29,30] and avalanche[31,32] photodiodes. The basic idea is to place the photodiode inside a Fabry-Perot resonant microcavity, so that the optical field builds up at resonant wavelengths. Enhancement of the optical field at resonant wavelengths allows us to use thinner absorbing layers, meaning that we can achieve higher bandwidths without sacrificing from quantum efficiency, leading to higher bandwidth-efficiency products. Such photodiodes are called resonant cavity enhanced (RCE) photodetectors and are promising candidates for high performance detection in optoelectronic integrated circuits (OEICs).

So what is the cost for this performance improvement? Firstly, a complex epitaxial design is required. Therefore the MBE growth of an RCE photodiode wafer is much more difficult than a conventional detector. It needs a very controlled and sensitive epitaxial growth. Hence an RCE photodetector is much more expensive. Another main drawback is the wavelength selectivity introduced by the resonant cavity. Although we obtain high efficiencies at resonant wavelengths, quantum efficiency at off-resonance wavelengths is suppressed. Actually this feature may be seen as an advantage for applications which require wavelength selectivity, such as wavelength division multiplexing (WDM) in optical communication systems.

2.3.1 RCE Photodiode Operation

Figure 2.7 shows the typical epitaxial structure of an RCE photodiode. The conventional photodiode with a thin absorbing region is placed inside a Fabry-Perot microcavity. The front and back mirrors are distributed Bragg reflectors (DBRs) which consist of quarter wavelength thick alternating layers of non-absorbing larger bandgap materials. The incident optical field bounces back and forth between the mirrors, so that the photons at resonance are recycled. Hereby the effective absorbing layer thickness is increased and high quantum efficiencies
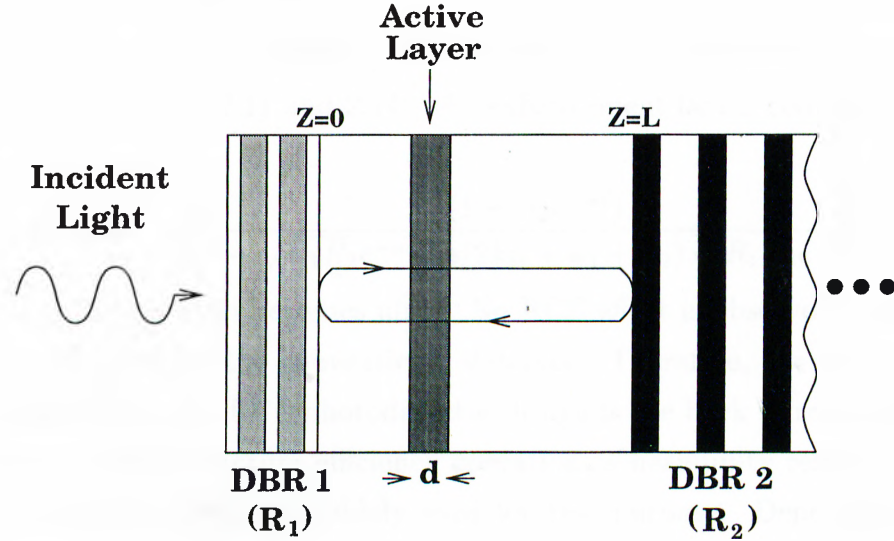
Figure 2.7: Typical RCE photodiode structure. Front and back mirrors are DBRs designed for operation wavelength.

can be obtained. Assuming no RC limitation (since a small d is used), the carrier transit times decreases, so that faster operation becomes possible. Hence, with this structure both high speed and high quantum efficiency photodetection can be achieved.

The quantum efficiency expression for an RCE photodiode with lossless cavity and mirror layers is derived as,[11]

$$\eta = \left\{ \frac{(1 + R_2 e^{-\alpha d})}{1 - \sqrt{R_1 R_2} e^{-\alpha d} cos(2kL + \psi_1 + \psi_2) + R_1 R_2 e^{-2\alpha d}} \right\} (1 - R_1)(1 - e^{-\alpha d}) \tag{2.14}$$

where R_1 and R_2 are the front and back mirror reflectivities respectively, α is the absorption coefficient of the absorbing layer, d is the active layer thickness, k is the propagation constant, L is the cavity length and ψ_1 and ψ_2 are the phase shifts introduced by the front and back mirrors respectively. One can deduce very important design criteria from Equation 2.14.

2.3.2 Design Parameters

Comparing the quantum efficiency formulations of a conventional and an RCE photodiode (Equation 2.11 and 2.14), the enhancement factor comes out as,

$$Enhancement = \left\{ \frac{(1 + R_2 e^{-\alpha d})}{1 - \sqrt{R_1 R_2} e^{-\alpha d} cos(2kL + \psi_1 + \psi_2) + R_1 R_2 e^{-2\alpha d}} \right\} \quad (2.15)$$

When $R_2 = 0$, this term becomes unity. No RCE effect is observed in this case, which is equivalent to the conventional detector. Therefore, the most crtitical design parameter in an RCE photodetector design is the back mirror reflectivity, R_2. For near unity quantum efficiency operation, a near unity reflectance back mirror is needed. DBRs are widely used for this purpose. Depending on the materials used, mirrors with reflectivities for desired spectral ranges beyond 99% can be designed. Front mirror reflectivity, R_1 and single pass absorption, αd are the other important design parameters. RCE effect is best observed for small single pass absorptions, with small d and moderate α values. R_1 can be optimized with respect to R_1 and αd, for maximum peak efficiency at resonance wavelength.

The enhancement term also indicates a periodic variation of quantum efficiency due to the term $cos(2\beta L + \psi_1 + \psi_2)$. η is enhanced periodically at resonant wavelengths which occur when $2\beta L + \psi_1 + \psi_2 = 2m\pi (m = 1, 2, 3, ...)$. This term introduces the wavelength selectivity of the RCE photodetector.

We analyzed the quantum efficiency spectrum of an RCE photodiode as a function of R_2, R_1 and αd and plotted the simulation results in Figure 2.8, 2.9 and 2.10. The simulations are done for an idealized RCE photodiode with $0.5\mu m$ cavity length, lossless cavity and wavelength independent mirror reflectivities. In Figure 2.8, we simulated the effect of back (bottom) mirror reflectivity, R_2 on the quantum efficiency spectrum, for $\alpha d = 0.1$ and $R_1 = 0.6$. The results show a strong dependence between R_2 and η. The flat response corresponds to the conventional photodiode with no bottom mirror ($R_2 = 0$). The quantum efficiency is below 5%, which the single pass absorption. η is enhanced at the resonant wavelengths as R_2 is increased. A maximum quantum efficiency of 85% is achieved with a nearly perfect ($R_2 = 0.99$) back mirror.
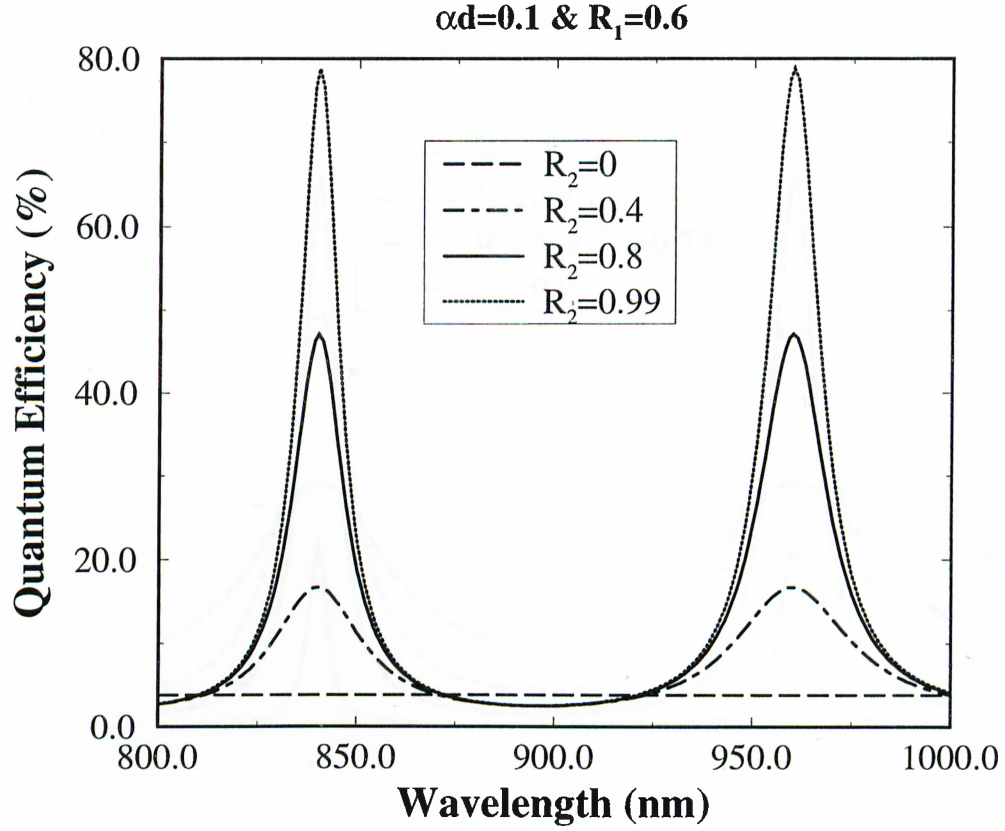
Figure 2.8: Quantum efficiency spectrum of an RCE photodiode as a function of bottom mirror reflectivity, R_2.

The quantum efficiency dependence on front (top) mirror reflectivity, R_1 is shown in Figure 2.9. For a given αd and R_2, there exists an optimum R_1 value, which can be derived from Equation 15. By taking the derivative of this expression with respect to R_1 and equating to 0, the optimum R_1 value is found as,

$$R_1 = R_2 e^{-2\alpha d} \qquad (2.16)$$

which corresponds to the perfect phase matching condition. We simulated the RCE structure for $\alpha d = 0.1$ and $R_2 = 0.9$. As we increased R_1 upto the matching
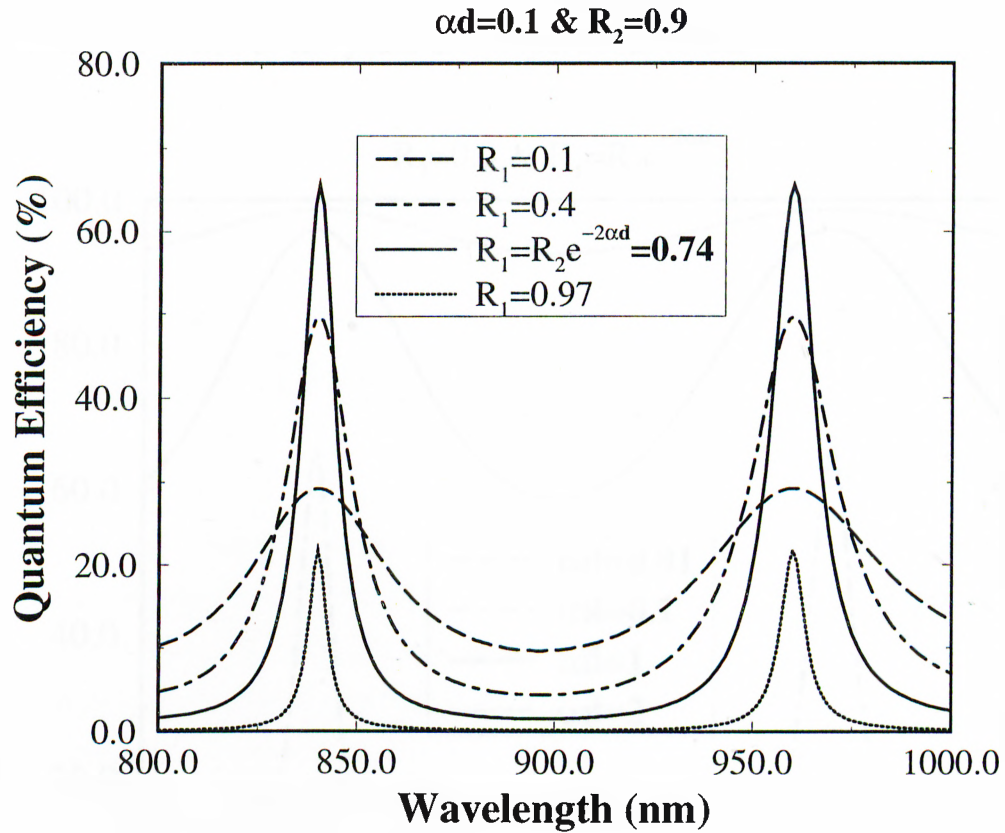
Figure 2.9: Quantum efficiency spectrum of an RCE photodiode as a function of front mirror reflectivity, R_1.

value, $R_1 = 0.74$, the peak η values improved. By further increasing R_1 we deviate from the matching condition, so that the quantum efficiency is decreased. Full width at half-maximum (FWHM) gets narrower as R_1 is increased.

The third design parameter, αd, is another important optimization term in RCE photodetection. Four different αd values are simulated with $R_2 = 0.9$ and $R_1 = R_2 e^{-2\alpha d}$ in Figure 2.10. Although η is increased at resonant wavelengths for higher αd values, RCE effect nearly disappears for $\alpha d > 2$, i.e. a flat, near unity quantum efficiency is observed for $\alpha d = 5$. In such designs almost all optical power is absorbed during the single pass, so that a little portion of the

optical field is recycled. Therefore the wavelength selectivity gets weaker as αd is increased. FWHM of the peaks are proportional to αd.

$$R_2 = 0.9 \ \& \ R_1 = R_2 e^{-2\alpha d}$$
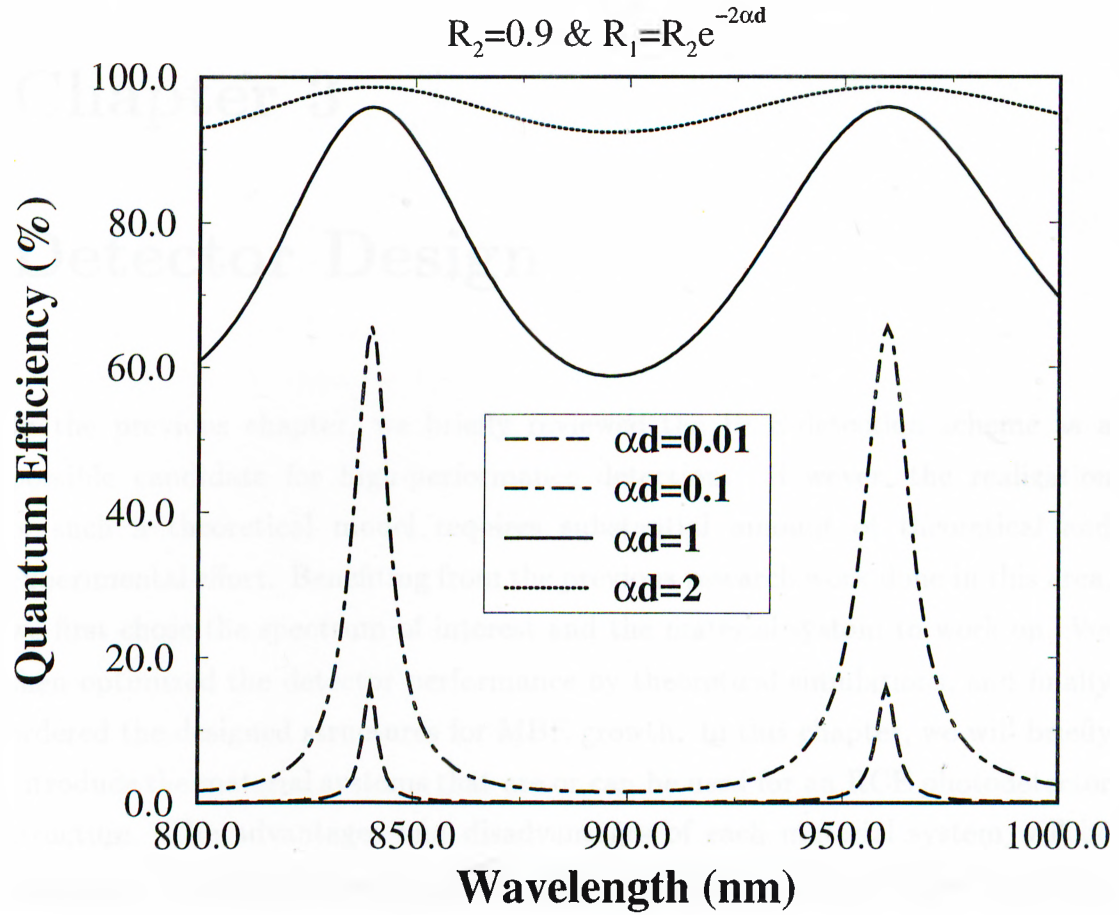
Figure 2.10: Quantum efficiency spectrum of an RCE photodiode as a function of αd.

Chapter 3

Detector Design

In the previous chapter, we briefly reviewed the RCE-detection scheme as a possible candidate for high-performance detection. However, the realization of such a theoretical model requires substantial amount of theoretical and experimental effort. Benefiting from the previous research work done in this area, we first chose the spectrum of interest and the material system to work on. We then optimized the detector performance by theoretical simulations, and finally ordered the designed structures for MBE-growth. In this chapter, we will briefly introduce the material systems that are or can be used for an RCE photodetector structure. The advantages and disadvantages of each material system will be discussed. Afterwards, the simulation method - Scattering Matrix Method - that we used to simulate and optimize the photodiode performance will be reviewed. We will then explain the optimized Schottky and p-i-n photodiode designs. The reflectivity measurements of the MBE-grown samples will be compared with our theoretical simulations. Finally, the wavelength tuning of the as-grown samples using a recess etch will be described.

3.1 Material Systems for RCE-Photodetectors

Optical frequencies cover a significant portion of the electromagnetic spectrum, starting from the ultra-violet (UV) and extending to the far infrared. Each

spectrum range has its specific applications: UV for military applications, visible and near infrared for optical fiber communication, mid- and far-infrared for sensing and medical applications. There is an enormous commercial investment on optical fiber communication which relies on optoelectronic components working at optical communication window wavelengths. These wavelengths are $0.85\mu m$, $1.3\mu m$ and $1.55\mu m$, denoting the first, second and third communication windows for optical fibers respectively. While the $0.85\mu m$ window was the first one used in fiber-optic communication, the transmission medium(glass fiber) has the largest attenuation with respect to the other two windows. At $\lambda = 1.3\mu m$, the fiber demonstrates near-zero dispersion by cancelling the material and waveguide dispersion at this wavelength but shows larger attenuation than the third communication wavelength, $\lambda = 1.55\mu m$. At $\lambda = 1.55\mu m$, the optical signals traveling through the fiber medium see minimum attenuation. This results in a lesser number of repeaters, and hence a smaller cost for the signal transmitted over the same distance.[33]

The performance of an optical communication system is measured with its bandwidth-cost product. To increase this product there is demand for high-performance system components, including photodetectors, operating at these optical fiber communication wavelengths. We know that RCE photodetectors offer this high-performance along with high quantum efficiencies. From an experimental point of view, one can summarize the features of a proper material system for RCE-detection as the following:

- Lattice matching between the materials

- Low-loss cavity (non-absorbing cavity and mirror materials)

- High-reflectance bottom mirror (DBR)[34]

- Moderate active layer absorption coefficient

Fortunately several material systems fulfill most or all of these requirements in different optical communication windows.[11] Let's have a brief look at the

alternative material systems for RCE-detection and criticize them with respect to the requirements listed above:

1. **AlGaAs/GaAs:** The MBE growth of this material system is relatively easy, since there is an excellent lattice match between GaAs and AlAs. GaAs is used as the active layer which has moderate absorption coefficient and demonstrate good carrier transport characteristics. Also the relatively high refractive index contrast between GaAs and AlAs results in near-unity reflectivity DBR mirrors. However the bandgap of GaAs lies around $0.87\mu m$, meaning that we can operate only in the first optical communication wavelength, $\lambda = 0.85\mu m$. Low-loss cavity formation is possible by using $Al_xGa_{1-x}As$ cavity layers and $Al_xGa_{1-x}As/AlAs$ alternating layers for bottom DBR.

2. **AlGaAs/GaAs/InGaAs:** This material system extends the operation wavelength of the above material system by incorporating $In_xGa_{1-x}As$ active layer instead of GaAs. As the In concentration increases the bandgap of the active material decreases, so that detection at longer wavelengths become possible. But still one cannot go to the 2nd and 3rd optical communication windows with this material system, since it is very hard to grow In_xGa_{1-x} active layer on $Al_xGa_{1-x}As$ due to the lattice mismatch between these materials. Although $In_{0.53}Ga_{0.47}As$ has the ability to absorb light at $1.3\mu m$ and $1.55\mu m$, it should be grown on a substrate different than GaAs. High-performance RCE photodiodes operating around 900 nm have been demonstrated using this material system[27,35]

3. **InP/InGaAs/InAlAs:** If InP is used as a substrate for $In_{0.53}Ga_{0.47}As/In_{0.52}Al_{0.48}As$ alloy system, excellent lattice matching and electrical properties with moderate absorption coefficient for RCE-detection at $1.3\mu m$ and $1.55\mu m$ become possible. The main disadvantage of this material system is the low refractive index contrast between InGaAs and InAlAs which increases the number of periods required for a good bottom DBR. Even if this problem is solved by careful MBE growth,

still one cannot form low-loss cavities using this material system since InGaAs layers forming the cavity and bottom mirror have absorption at the wavelengths of interest. To overcome this drawback, transparent GaAs/AlAs bottom mirrors can be wafer-fused to the Fabry-Perot microcavity.[36,37] This material system is one of the best candidates for RCE-detectors that can be used in fiber-optic communications.

4. **Si/SiGe:** The most important advantage of this material system is the integrability with the well-developed silicon-based electronics. $Si/Si_{0.8}Ge_{0.2}$ combination is lattice matched up to a thickness of $0.1\mu m$, and this limit allows MBE growth of DBRs for $\lambda = 1.55\mu m$ using this material system.[38] The main drawbacks are similar to the ones faced with InP/InGaAs/InAlAs material system: poor refractive index contrast leading to low performance bottom DBR and absorbing cavity and mirror layers make difficult to form low-loss cavities. Also, Si and Ge are indirect-bandgap materials, meaning smaller absorption coefficients and therefore reduced RCE-performance. However, successful RCE detectors are reported with this material system at shorter wavelengths around 700 nm.[39,40]

5. **Ternary and Quaternary Material Systems:** In recent years with the enormous development in VCSELs (vertical cavity surface emitting lasers) new material systems are developed for optical communication wavelengths. The aim was to overcome the low index contrast and lossy cavity problems at $1.3\mu m$ and $1.55\mu m$. Some examples which offer potential are InGaAsP/InP,[41] AlGaAsSb/AlAsSb, AlGaInAs/AlAsSb.[42] For shorter wavelength operation AlGaInP/GaInP, AlGaP/GaP, AlGaAs/Al-oxide are promising materials for high-performance optoelectronic applications including RCE-detection. Especially GaAs/Al-oxide DBRs offers excellent bottom mirrors with smaller number of periods.[43]

Optical fiber communication systems operating at $1.3\mu m$ and $1.55\mu m$ are used for wide area networks (WANs), long-haul and sub-marine systems which connect cities, countries and continents. Then the question is: Is there still

need for GaAs-based systems working at $\lambda = 0.85 \mu m$? The answer is yes, but not in long-distance communication. Systems working around the first optical communication window are widely employed in local area networks (LANs) where the attenuation in optical fiber becomes tolerable. AlGaAs/GaAs and AlGaAs/GaAs/InGaAs material systems are the best choices for this operation wavelength. Besides the excellent features we have discussed previously, its compatibility with GaAs fabrication technology and the existence of a developed fabrication process for GaAs-based photodetectors makes the AlGaAs/GaAs material system attractive for RCE-photodetection. Hence, our motivation in this work is to demonstrate high-performance RCE photodetectors working at the first optical communication wavelength using the AlGaAs/GaAs material system.

3.2 Device Simulation

A powerful simulation technique is vital to make proper designs. Since our detector designs are rather complicated and difficult to grow -therefore expensive-, we should be able to analyze and optimize our designs well before ordering them for MBE-growth. An RCE photodetector structure consists of multilayer optical films, and therefore we need a simulation method by which we can analyze the optical field in such multilayer structures. Several simulation techniques, including the scattering matrix method (SMM), offer a systematic approach to analyze multilayer structures. We have used the S-matrix method in our simulations which was developed by Mutlu Gokkavas.[44] This method provides a simple technique to calculate the exact field distribution within the cavity.

Of course simulations assume somewhat ideal conditions. When employing the S-matrix method to simulate our designs some assumptions are made. First of all, the incoming light is assumed to be a monochromatic plane-wave. Second, these plane-waves are assumed to reach the detector surface with normal incidence, so that reflections from all interfaces inside the cavity can be calculated using Fresnel's coefficients. Another idealization is the perfect

interface assumption between different material layers. However, this is never the case in a real MBE-grown sample. Structures are assumed to have no defects and the diffraction of the optical field near the boundaries are omitted, i.e. the layers extend over the entire plane of normal incidence. So, propagating the optical field through multilayer structure becomes a one-dimensional problem which simplifies our calculations.
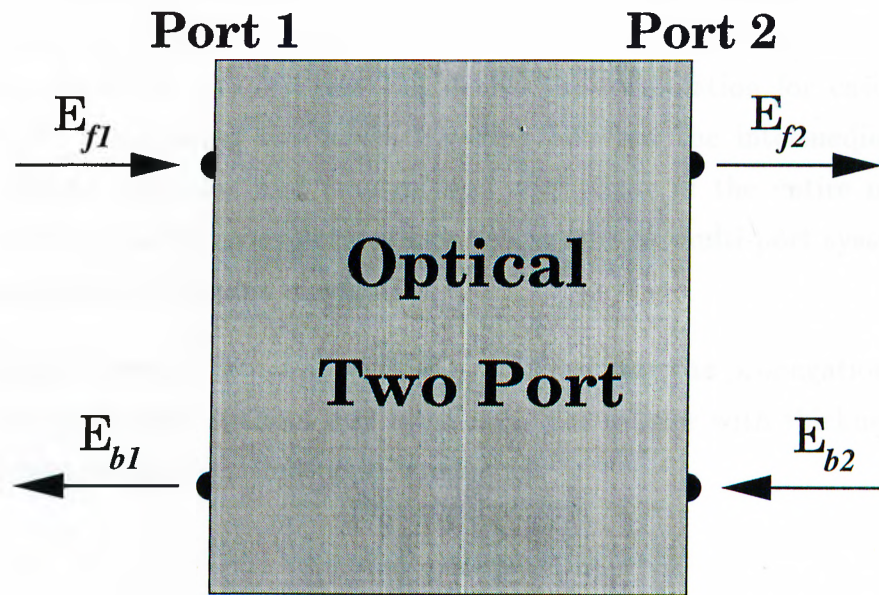
Figure 3.1: Traveling waves entering and leaving an optical two port layer.

The S-matrix method we have used in our simulations is nothing but an analogy of transmission-line theory. Each layer in the multilayer stack corresponds to a two-port transmission line with a normalized characteristic impedance $Z = 1/n$, where $n = n_R + i n_I$ denotes the complex refractive index of the layer material. n_R and n_I represent the real and complex part of the refractive index respectively. Traveling waves are used in transmission-line theory to characterize the two-ports in terms of S-parameters. S-parameters of a two-port system represent the waves leaving the two-port in terms of the waves entering the two-port. These traveling waves are shown in Figure 3.1, where E_{f1} and E_{b2} denote the incident waves, and E_{b1}, E_{f2} the leaving waves. Since

the wave-equation is linear, using the superposition principle, one can write the output variables as a linear superposition of the input variables:

$$\begin{bmatrix} E_{f2} \\ E_{b1} \end{bmatrix} = \begin{bmatrix} t_{12} & r_{21} \\ r_{12} & t_{21} \end{bmatrix} \begin{bmatrix} E_{f2} \\ E_{b1} \end{bmatrix} ,$$ (3.1)

where t_{ij} and r_{ij} represent the field-transmission and field-reflection coefficients for waves traveling from port i to port j. The matrix corresponds to the S-matrix of this two-port element.

Using signal-flow graphs, one can derive the formulation for cascading S-matrices.[45] Eliminating the waves traveling between the intermediate ports, we can obtain reflection and transmission coefficients of the entire multilayer stack. Optical multilayer structures can be thought as multi-port systems with 2 different kind of two-port elements:

- **Single Layer** : Denoted with S_{layer}. Represents the propagation of light in a single layer without any interfaces. For a layer with thickness d, the corresponding S_{layer}-matrix is written as

$$S_{layer} = \begin{bmatrix} e^{ikd - \frac{\alpha}{2}d} & 0 \\ 0 & e^{ikd - \frac{\alpha}{2}d} \end{bmatrix} ,$$ (3.2)

  where $k = 2\pi n_R/\lambda$ and $\alpha = 4\pi n_I/\lambda$ are the propagation and attenuation constants respectively, and λ is the free-space wavelength of the incident light field. No reflections occur, therefore $r_{ij} = 0$. If $\alpha \neq 0$, then the propagating light waves will undergo a magnitude modification besides a phase shift due to propagation inside the medium.

- **Interface** : This kind of two-port element corresponds to a physical boundary between two different materials. $S_{interface}$ is totally determined by Fresnel's reflection and transmission coefficients for normal incidence:

$$S_{interface} = \begin{bmatrix} \frac{2n_1}{n_1 + n_2} & \frac{n_1 - n_2}{n_1 + n_2} \\ \frac{n_2 - n_1}{n_1 + n_2} & \frac{2n_2}{n_1 + n_2} \end{bmatrix} ,$$ (3.3)

where n_1 and n_2 are the complex refractive indices of the two neighbor layers. Ideal interfaces have no thicknesses, therefore the field phasers don't change. At limiting case, when $n_1 = n_2$, $S_{interface}$ becomes equal to S_{layer} for $d = 0$.

S_{layer} and $S_{interface}$ are the building blocks of our calculations. Using S_{layer}, $S_{interface}$ and the rules for cascading S-matrices, S-parameters (transmission and reflection coefficients) of any passive multilayer stack can be determined. The only data we need is the complex refractive index data of the materials used in the stack, which is well-documented for AlGaAs/GaAs material system.[46]

When we measure the reflectivity of a sample, we measure the power reflectivity, not the field-reflectivity. The same is valid for transmittivity. Using the following formulas, field coefficients are converted to power coefficients:

$$R_{ij} = |r_{ij}|^2 \tag{3.4}$$

$$T_{ij} = \frac{n_j}{n_i}|t_{ij}|^2 \tag{3.5}$$

Calculation of absorption is another important calculation for optimizing the quantum efficiency of the design. With S-matrix approach, absorption in single/multi layers can be calculated using the following procedure. The optical power entering and leaving the absorbing layer(s) is calculated and differentiated so that the remaining amount is the power absorbed in the absorbing region. In other words, one should differentiate the power transmitted to the right side of the absorptive layer(s) and the power transmitted to the left side of the absorptive layer(s). Hence, S-matrix method allows us to simulate the reflection, transmission and absorption spectrums of our optical multilayer design structures.

As stated earlier, it is desired to have a perfect bottom mirror for high-performance RCE-detection. Metals are known as good reflecting materials. However they are not perfect mirrors ($R < 96\%$), and show variance along the spectrum. Another major disadvantage of metal mirrors is that they are strong absorbers at optical frequencies, so that low-loss cavities can't be formed with
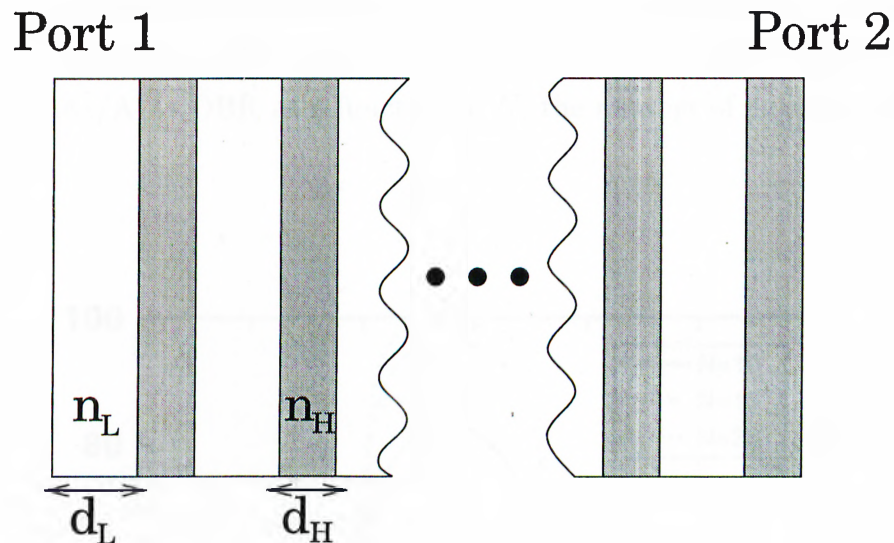
Figure 3.2: Quarter wave stack as a two port.

these mirrors. Instead DBRs are used widely in optoelectronic applications. A DBR is a periodic stack with two alternating quarter-wave thick materials (Figure 3.2). n_H and n_L are the complex refractive indices of the high-index and low-index material respectively. λ_c is the design wavelength of the mirror. Applying the S-matrix method to this structure the peak power reflectivity at central wavelength comes out as

$$R_{peak} = \left\{ \frac{n_H^{2N} - n_L^{2N}}{n_H^{2N} + n_L^{2N}} \right\}^2 \tag{3.6}$$

where N is the number of mirror-pairs in the stack, n_H and n_L are the complex refractive indices of the high-index and low-index material respectively. For a constant period number N, the critical design parameter is the refractive index contrast between the mirror materials, $\Delta n = n_H - n_L$. With higher contrast mirror layers we can achieve higher reflectivities for the same N. GaAs/AlAs DBR offers the maximum index-contrast for the material system used, but is not suitable for design wavelengths shorter than $0.87 \mu m$. Therefore for a DBR design at $0.84 \mu m$, it is preferable to use $Al_{0.2}Ga_{0.8}As$ and AlAs as mirror materials. The

bandgap of $Al_{0.2}Ga_{0.8}As$ lies around $0.75\mu m$ so that we can get rid of absorption in mirror layers. Figure 3.3 shows the simulation of the reflectivity spectrum of a $Al_{0.2}Ga_{0.8}As$/AlAs DBR as a function of N, the number of periods of DBR.
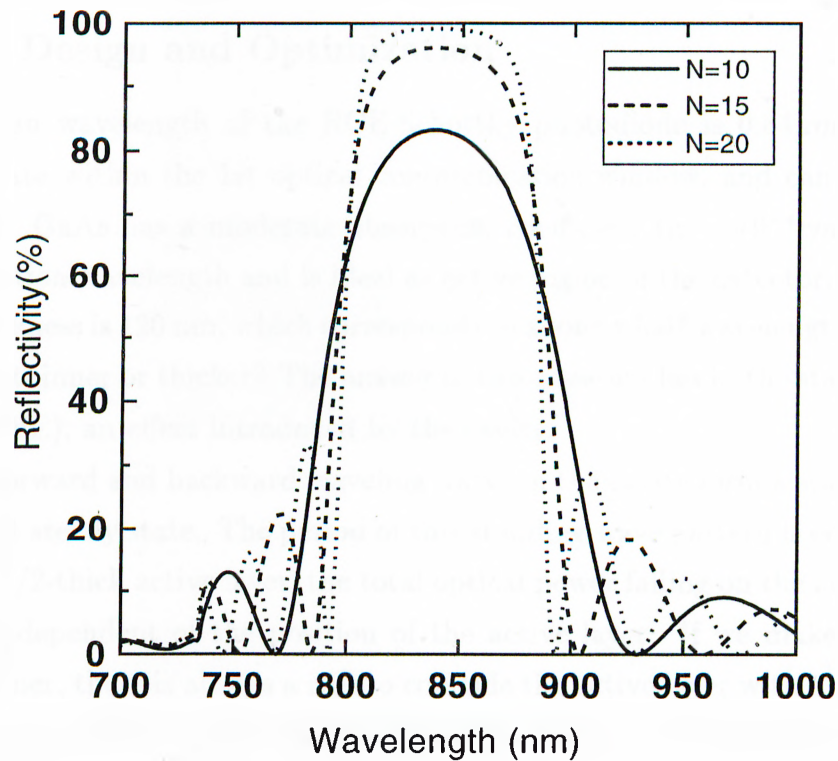
Figure 3.3: Reflectivity spectrum of $Al_{0.2}Ga_{0.8}As$/AlAs DBR for N=10, 15 and 20. Design wavelength is 840 nm.

As N increases, the reflectivity increases and reaches 99% for $N = 20$. So, in order to have a significant RCE effect, a bottom DBR with $N \sim 20$ is needed. It is preferable to have a 30 or 40 period bottom DBR, but this increases the cost of the MBE growth. In the following sections the RCE-photodetector designs that we worked on will be introduced: RCE Schottky and RCE p-i-n photodetector designs.

3.3   Schottky Design

As discussed in Chapter 2, Schottky photodiodes can achieve very high operation bandwidths since they are majority carrier devices. But these devices lack from poor quantum efficiencies. The design shown in Figure 3.4 is made to overcome this handicap without sacrificing from operation speed.

3.3.1   Design and Optimization

The design wavelength of the RCE-Schottky photodiode is $0.84\mu m$ so that it can operate within the 1st optical communication window, and can be utilized in LANs. GaAs has a moderate absorption coefficient ($\alpha \sim 10^{-4}cm^{-1}$) around the operation wavelength and is ideal as active region of the detector. The active layer thickness is 120 nm, which corresponds to about a half-wavelength thickness. Why not thinner or thicker? The answer of this question lies in the standing wave effect (SWE), an effect introduced by the cavity.

The forward and backward traveling waves in the cavity form a standing wave pattern at steady state. The period of this standing wave pattern is equal to $\lambda/2$. So for a $\lambda/2$-thick active layer, the total optical power falling on the active region will be independent of the position of the active layer. If we make the active layer thinner, there is always a risk to coincide the active layer with a node of the standing wave which can be caused by growth variations. The quantum efficiency then can decrease dramatically. Of course, it is much better to use a thinner active region that coincides with a maximum of the standing wave pattern. This will improve the performance of the device, especially the bandwidth which will increase as the active layer gets shorter. But, this approach needs a very well controlled MBE growth and is much more sensitive to growth rate fluctuations. Therefore, it is safer to have a an active layer with $\lambda/2$ thickness. Thicker active layers can also be used, at the expense of a decrease in the speed performance of the diode.

In order to have a low-loss cavity, $Al_{0.15}Ga_{0.85}As$ and $Al_{0.2}Ga_{0.8}As$ are used for intermediate cavity materials. Semi-insulating GaAs is used as the growth

80 nm	$Al_{0.15}Ga_{0.85}As$	N^-	doped
30 nm	Graded Interface	N^-	doped
120 nm	GaAs (Active Layer)	N^-	doped
30 nm	Graded Interface	N^-	doped
160 nm	$Al_{0.2}Ga_{0.8}As$	N^-	doped
400 nm	$Al_{0.2}Ga_{0.8}As$	N^+	doped
230 nm	$Al_{0.2}Ga_{0.8}As$		undoped

19 Pairs of

$Al_{0.2}Ga_{0.8}As$ / AlAs

Distributed Bragg Reflector

Semi-Insulating GaAs Substrate

Figure 3.4: Epitaxial design of RCE Schottky photodetector.

substrate. Bottom mirror consists of a 18.5 period $AlAs/Al_{0.2}Ga_{0.8}As$ Bragg mirror designed at 840 nm. The 230 nm thick undoped $Al_{0.2}Ga_{0.8}As$ layer on top of the bottom DBR is the mesa isolation region of our diodes. Then comes the n^+ region, which is called as the ohmic layer. Ohmic contacts of the photodiodes are made within this 400 nm thick layer. This is followed by a 160 nm thick n^- buffer layer. On each side of the active layer, graded interfaces are employed. Sharp interfaces, i.e. interfaces without graded regions, cause carrier trapping problems near the interface. To get rid of this performance reduction, smooth interfaces are preferred in heterojunction devices. In our design, two graded interface regions are used to increase the detector performance. The graded regions are 30 nm thick and n^- doped. The top layer of the cavity is a 80 nm thick n^- doped $Al_{0.15}Ga_{0.85}As$ layer. By etching this layer, one can tune/shift the resonance wavelength.

The top mirror of the cavity will be formed by a thin, semi-transparent Au layer which will also function as the Schottky-metal. The optimum Au thickness is found to be around 100 Angstrom. Actually Au is not an ideal top mirror since it is absorbing. But, it shows very good electrical properties and forms excellent Schottky contacts. Another disadvantage of using Au as top mirror is its growth chemistry. When Au is deposited on the semiconductor surface, it builds up in island-forms. This growth mechanism results in a rough surface. AFM studies in Boston University showed that the surface roughness was nearly comparable with the Au thickness! Such a surface cause scattering of the incident optical field, which will degrade the detector performance.

Another design criteria was to take the different carrier velocities into account. Since the holes will drift to the Schottky metal and the electrons to the ohmic contact. The absorption layer is placed closer to the Schottky metal, so that the transit times for holes and electrons are equalized.

3.3.2 Reflectivity Characterization

Before the fabrication process, we first measure the reflectivity spectrum of the MBE-grown wafer. One can deduce very useful results by comparing the reflectivity measurement results with theoretical predictions. In Figure 3.5, measured and simulated reflectivity spectra are shown.

We fitted the simulation curve to the experimental result by making minor changes in the structure. Active region thickness is reduced from 120 nm to 100 nm, while 20 nm is added to the top layer. An additional 10 nm is removed from the bottom AlGaAs layer. We also increased the mirror layers by 1% i.e, red-shifted the mirror. The comparison of measurement and theory indicates a growth imperfection around 1%.

3.3.3 Wavelength Tuning

By changing the cavity length we can shift the resonant wavelength of the detector.[47] We can shorten the cavity by a recess etch of the top $Al_{0.15}Ga_{0.85}As$
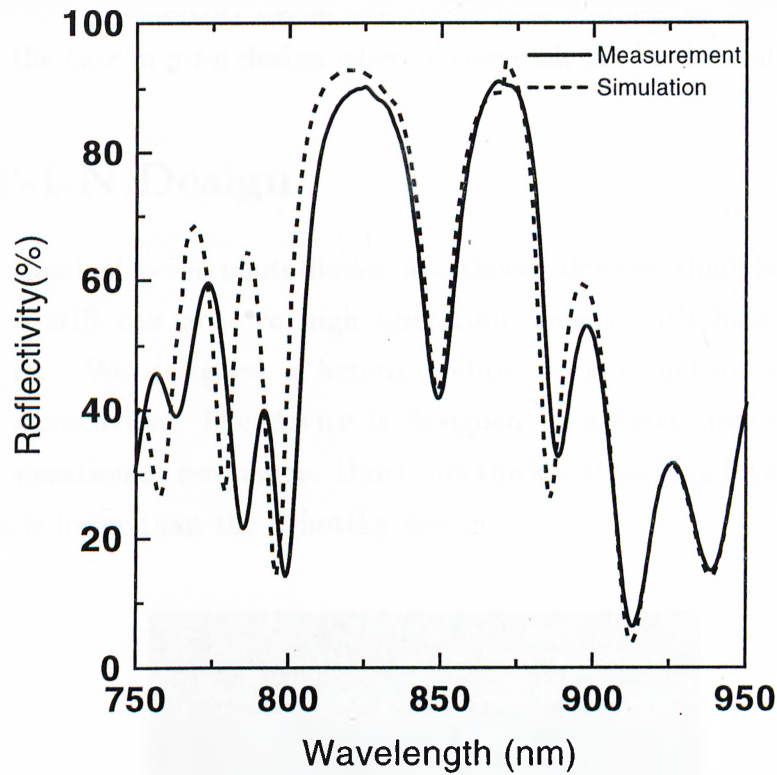
Figure 3.5: Measured and simulated reflectivity spectrum of RCE Schottky photodetector design.

layer. This leads to a blue-shift of the resonant wavelength. From the simulations we deduced that for a 10 nm shift in the resonant wavelength, we need to etch about 20 nm from the top layer. Fortunately, the MBE wafer was grown excellently and no recess etch was needed before fabrication process. We also examined the diode working at the second resonant wavelength. We etched the top layer in small steps and controlled the wavelength-shift by the reflection set-up. We have stopped the recess etch when the second resonance reached 850 nm, so that after Schottky metal deposition our resonance would appear around 840 nm.

An important point for the Schottky design is that the wavelength tuning should be done before fabrication. After the fabrication process, the top layer will be covered by the Schottky metal and recess etch will not be possible. However, this is not the case in p-i-n design where recess etch can be done after fabrication.

3.4   P-I-N Design

Although classical p-i-n photodiodes are slower devices than Schottky photodiodes, one still can achieve high operation speeds with heterojunction p-i-n structures. We designed a heterojunction p-i-n structure embedded in a resonant microcavity. The device is designed to achieve near-unity quantum efficiency operation at resonance. Due to its thicker absorbing layer, the expected bandwidth is lower than the Schottky design.

20 nm	GaAs	P^+ doped
200 nm	$Al_{0.2}Ga_{0.8}As$	P^+ doped
38 nm	Graded Interface	undoped
470 nm	GaAs (Active Layer)	undoped
38 nm	Graded Interface	undoped
390 nm	$Al_{0.2}Ga_{0.8}As$	N^+ doped
180 nm	$Al_{0.2}Ga_{0.8}As$	undoped

24 Pairs of

$Al_{0.2}Ga_{0.8}As$ / AlAs

Distributed Bragg Reflector

Semi-Insulating GaAs Substrate

Figure 3.6: Epitaxial design of RCE P-I-N photodetector.

3.4.1 Design and Optimization

Figure 3.6 shows the final epitaxial design for the RCE p-i-n photodiode. The design wavelength is 820 nm. As in Schottky design, a semi-insulating GaAs substrate is used. To achieve near-unity quantum efficiency, the number of periods of the bottom DBR is increased from 18 to 24. An undoped buffer layer of 180 nm for mesa isolation is followed by a 390 nm thick n^+-doped layer which acts as the cathode. Similar to the Schottky structure, graded interfaces are used on each side of the active intrinsic region. The GaAs active layer is four times thicker than the Schottky design, resulting in increased single pass absorption and longer transit times. The anode of the diode is formed by a p^+-doped $Al_{0.2}Ga_{0.8}As$ layer and a thin GaAs top layer. The total thickness of the p-region is 220 nm. Thin GaAs top layer is used to achieve good p-type ohmic contact.

Except the top GaAs layer, the cavity can be assumed to be lossless, since $Al_{0.2}Ga_{0.8}As$ is transparent for wavelengths greater than 750 nm. The top mirror is formed by air-GaAs interface, which gives a top mirror reflectivity $R_1 \sim 30\%$. Both mirrors are transparent and this results in improved quantum efficiency. Since we are primarily concerned in high quantum efficiency, the structure is not optimized with respect to the drift velocities of the photogenerated carriers.

3.4.2 Reflectivity Characterization

Simulation results show that near-unity quantum efficiency should be possible. The excellent dip in the reflectivity spectrum indicates this result. If nothing reflects back at resonance, this means that all of the optical power is either absorbed in the absorbing layers or transmitted through the bottom DBR. The simulations show that at resonance there is no transmission at all, and that almost all power is absorbed inside the cavity. The reflectivity measurement and simulation spectra are shown in Figure 3.7. The reflectivity dip shows little variance from the center to the edge of the wafer. We measured a minimum of 5% near the center of the epitaxial wafer. The measurement results indicates
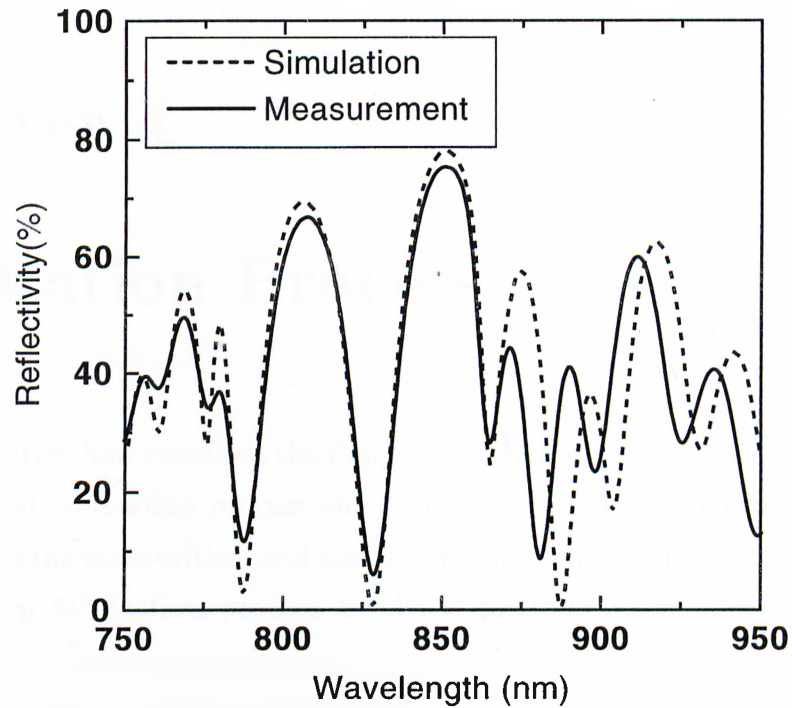
Figure 3.7: Measured and simulated reflection spectra of RCE p-i-n photodetector.

that a quantum efficiency of maximum 95% can be achieved.

3.4.3 Wavelength Tuning

Pre-fabrication recess etch is not applied for this design. As shown in Figure 3.7, the resonant wavelength coincides with the design wavelength, so there is no need for a shift in the resonant wavelength. Also, if the top GaAs layer is removed by recess etching, the p^+ ohmic quality will be probably reduced which lowers the detector performance. Recess etch is done after fabrication process is completed. These results will be discussed in detail later in Chapter 5.

Chapter 4

Fabrication Process

It doesn't matter how excellent the design and MBE growth is, unless you have a well-developed fabrication process and good fabrication experience. Fabricating the samples is the most critical and time consuming part of our work. Fortunately, a step-by-step fabrication process for RCE photodetectors already has been developed by other post-graduate students in our laboratory.[48,49] However, during the training and process development period we faced some vital problems which had to be solved. Fabrication is done in a class-100 cleanroom environment at the Advanced Research Laboratory of Physics Department. The process is a rather complicated, seven-step process which will be described in detail in this chapter. Before explaining the fabrication steps, the standard semiconductor processes will be introduced.

4.1   Standard Semiconductor Processes

4.1.1   Cleaving and Cleaning

It is easier to handle and safer to process small samples than the whole wafer. Therefore expensive MBE-grown wafers are cleaved into small samples before fabrication. Sample sizes around 8x8 mm were ideal to work with a 7x7 mm mask size. A diamond tipped scriber-pen is used to cleave the wafer along its

crystalline directions.

Each process step begins/ends with a standard cleaning process, called three solvent cleaning (TSC). Wafers are immersed in three different solvents sequentially: 2 minutes in boiling trichloroethane (TCA), 5 minutes in room temperature acetone and finally 2 minutes in boiling isopropanol. TSC is finished by rinsing the samples in deionized (DI) water flow, drying with nitrogen gun and a dehydration bake at 120 °C for 2 minutes at the hot plate. An optical microscope is used to inspect the sample surface.

4.1.2 Photolithography

Photolithography (PL) is the name of the most basic and important semiconductor process. Basically with PL, the mask pattern is transferred onto the sample surface. Each step has a different mask, hence in every step PL is applied. Therefore good quality PL is required for successful fabrication. In the following paragraphs we describe the steps followed in a standard PL.

First, the sample surface is covered with an adhesion promoter and afterwards with photoresist, which is a radiation-sensitive material, and is spanned for 40 seconds at 5000 rpm. We used AZ 5214E type photoresist, which is actually a positive resist, but can also be used as a negative resist.[50] With 5000 rpm spin rate, we ideally obtain a resist thickness of $1.4 \mu m$. Adhesion promoter, (chemical name is HMDS) is a liquid material which provides a better adhesion of the photoresist to the sample surface. Photoresist covered samples are baked on a hot plate at 110 °C. This bake is known as the pre-bake, since it is done before the exposure of the sample.

Photolithography can be divided into two categories: i) Normal PL ii) Image Reversal PL. The photoresist film is processed in two different ways leading to exactly reverse pattern transfers.

- **Normal Photolithography :** After pre-bake, the sample is aligned with respect to the mask, and exposed under UV-lamp at 365 nm for 30 seconds. A Karl-Suss MJB3 mask aligner is used for this purpose, and the mask

pattern of interest is transferred to the photoresist film.

- **Image Reversal Photolithography** : Similarly the photoresist covered sample is aligned and exposed using the mask aligner, but with a different mask and a shorter exposure time of 20 seconds. For the same mask level used for normal PL, the image reversed mask is used. So how can we get the same patterns? The answer is with an additional bake and exposure. We bake the exposed sample at 110 °C for 2 minutes, and make a flood UV exposure of the whole sample surface without using a mask for 40 seconds. These two extra processes change the chemistry of the photoresist so that image exposed (first exposure with mask) areas behave as non-exposed regions. The most critical step in image reversal PL is the additional bake, which is called as image reversal bake. We had to optimize the bake temperature and duration. This optimization is done using several dummy samples and applying different image reversal bake times and temperatures. Also image and flood exposure times were optimized during this process development. Image reversal PL helped us a lot by overcoming the lift-off problem of thick metalizations.

For development of the aligned and exposed samples, AZ 400K developer is used with a 1:4 ratio (developer:H_2O). The developer etch the exposed photoresist regions (reverse for image reversal procedure), so that desired geometric patterns are opened. One can observe the development of the photoresist by its continuously changing color. When the color changing has stopped and the grey color of GaAs has appeared, the sample is rinsed under flowing de-ionized (DI) water. After drying with nitrogen gas, the sample is examined under an optical microscope. The resolution patterns should be sharp, and $\sim 1\mu m$ resolution should be observable for a good PL. Also the alignment should be checked by examining the alignment marks.

4.1.3 Etching

Etching process is generally used for transforming the defined patterns by PL onto underlying semiconductor or dielectric layers, so that the desired layer for subsequent process (metalization, isolation, etc.) is reached. It is also used for thinning the photoresist film and cleaning the the surface regions to be etched. Mainly two types of etching is used in semiconductor processes: wet etching and reactive ion etching (dry etching).

1. **Wet Etching** : Chemical solvents are used to etch semiconductor and dielectric materials. Several solvents can be used as etchants for GaAs-related materials. The etchant consist of three components: an oxidizing agent, an acid or base, and DI water. Hydrogen peroxide (H_2O_2) is a good oxidizing agent and oxidizes the semiconductor surface. The oxidized layers (Ga_xO_y, As_xO_y, Al_xO_y) are removed by the acid or base such as sulfuric acid (H_2SO_4) or ammonium hydroxide (NH_4OH) so that semiconductor surface is etched. Dielectric materials such as S_3iN_4 and SiO_2 can also be wet etched using dilute hydrofluoric acid ($HF:H_2O$). One can adjust the etch rates from few angstroms to tens of nanometers per second by changing the solvent ratios. Before etching, a 60 second post-bake at 120 °C helps the photoresist to adhere to the sample perfectly and improves the etch quality.

2. **Reactive Ion Etching** : Reactive Ion Etching (RIE) is also known as dry etching. Photoresist films and dielectrics are etched with plasma ions hitting the sample surface. An ultra high vacuum (UHV) RIE machine is used for this purpose. With different gases, different materials can be etched. We used O_2 plasma to thin the photoresist film and to clean the sample surface before wet etching if necessary. O_2 is ideal for this purpose since it does not etch the semiconductor surface. Si_3N_4 can also be etched with RIE by using CHF_3.

4.1.4 Metalization

Schottky, ohmic, interconnect and airbridge metals are all formed by metal deposition. The metals are deposited onto the samples using an UHV box coater. Metals in solid or powder form are put into tungsten boats. The samples are fastened on a sample holder that is placed on top of the boats. After enough vacuum is created in the chamber, the desired metals are evaporated by passing currents through the tungsten boats. Each metalization has a different recipe with different evaporation rates and final metalization thicknesses vary at each step.

4.1.5 Rapid Thermal Annealing

Rapid thermal annealing (RTA) is a thermal process in which the samples are heated rapidly up to very high temperatures (max. 1400 °C) to form ohmic contacts. RTA is applied once in our fabrication process, after ohmic metalization. For annealing, we use an RTA device in which a flash lamp is embedded. The samples are heated under the radiation of the flash lamp for a certain time duration. Due to high temperature, ohmic alloy begins to melt, Ga diffuses into the metal and ohmic metals diffuse into the wafer, resulting in a ohmic contact at the metal-semiconductor surface.

4.1.6 Plasma Enhanced Chemical Vapor Deposition

Dielectric coatings are important for optoelectronic devices as they function as anti-reflection or reflection coatings. One method for dielectric film deposition onto semiconductors is plasma enhanced chemical vapor deposition (PECVD). This method allows low temperature and uniform film deposition, therefore is ideal for Si_3N_4 deposition in our fabrication process. Different dielectric films require different process gases. For Si_3N_4 deposition, silane ($2\%SiH_4 + 98\%N_2$) and ammonia (NH_3) gases are used to form a plasma in the process chamber at 250 °C.

4.1.7   Lift-off and Ultrasound application

Lift-off and ultrasound applications are used after the metalization processes. After metalization the samples are soaked into acetone. Acetone dissolves photoresist so that the parts of metal deposited on the photoresist will be lifted-off. On the other hand, the metal regions deposited onto the openings of the sample surface will stick to the surface. As a result, metal remains only on the desired openings at the sample surface, defined by the photomask. Especially for thick metalizations, if lift-off is not completed in acetone, ultrasound application is used to tear the metal pieces which have to be lifted off. But this is always a risky method since it can damage and tear the metal regions which should stay on the sample surface. Therefore it should be used very carefully and with short time durations.

4.2   Photodiode Fabrication Process

In this section, the step-by-step fabrication process is described. It consists of seven steps, i.e. seven mask levels are applied to the samples. Except one mask level (Schottky), the fabrication of p-i-n photodiodes is the same as Schottky photodiodes. First the Schottky photodiode fabrication steps are described and afterwards the different step for p-i-n photodiode is briefly explained.

4.2.1   Ohmic Contact Formation

After a normal PL, the opened areas are etched until the middle of n^+ region, using an ammonium hydroxide based etchant ($NH_4OH:H_2O_2:H_2O = 14:2.4:200$), which gives an etch rate around 50 Angstrom/sec. Since we should stop inside the n^+ layer, the overall etch is done in several steps, controlling the etch depth and etch rates after each step using a DekTak stylus profilometer. We etched $0.6\mu m$ and $0.95\mu m$ for Schottky and p-i-n structures respectively. When the desired etch depth is reached, ohmic metalization is done. Ge/Au/Ge/Au/Ni/Au are deposited with thicknesses of 108/102/63/236/100/3000 Angstroms, respectively.

When the lift-off is completed without any problem the samples are ready for RTA. Samples are annealed at 450 °C for 45 seconds. The quality of an ohmic contact can be understood by examining the sample under an optical microscope. The ohmic metals should display dark and light spots, i.e. swiss-cheese like features.

4.2.2 Mesa Isolation

This step consists of a normal PL followed by a wet-etch. Using the same etchant (used for ohmic-etch), we etch all the sample surface except the diode active regions, called mesas. To isolate these active regions, we have to reach the undoped layer below the n^+ ohmic layer. This is achieved by monitoring the etch depth using DekTak profilometer several times, until the undoped AlGaAs layer is reached. The desired etch depth is around $0.9 - 0.95 \mu m$ for Schottky design, and $1.25 - 1.3 \mu m$ for p-i-n design.

4.2.3 Interconnect Metalization

In order to connect the mesas to either transmission lines or microwave compatible pads, an interconnect metal layer is deposited over the undoped AlGaAs. This metal layer also functions as the lower plates of the metal-insulator-metal (MIM) capacitors. Image reversal PL is done before metalization, so that the desired undercut profile for good lift-off process is obtained. A thin (150 Angstrom) Ti layer is deposited to enhance the adhesion of the subsequent thick Au layer ($\sim 1 \mu m$). We faced thick-metal lift-off problems with normal PL. However after the development of image reversal PL, thick metals were lifted-off without any problem.

4.2.4 Schottky Metalization

The Schottky metal (Au) is deposited on top of the diode structure, so that it acts as the top mirror as well as the Schottky contact. Since Au is a highly absorbing

metal, a semi-transparent top mirror can be achieved by a relatively thin Au layer. Before metalization, normal PL is done with the Schottky mask. A 100 Angstrom-thick metal results in a good Schottky contact along with a moderate top mirror. The main disadvantage of this top mirror is the surface roughness which causes scattering of incident light. After the metalization the samples are soaked into acetone for lift-off. The lift-off in this step is usually achieved in a few minutes, since the metal is very thin.

4.2.5 Dielectric Deposition

A thin ($\sim \lambda/2$) PECVD grown Si_3N_4 film is deposited all over the sample surface. Using a normal PL and wet-etch, nitride film is etched away from the desired areas, i.e. air-post openings and end pads of interconnect metals for microwave probing. A diluted HF etchant (HF:H_2O = 1:40) is used for this purpose, which etches the whole nitride layer within 10-15 seconds. The desired openings are controlled under an optical microscope. The deposited nitride layer functions as an anti-reflection coating as well as the dielectric slab for the MIM capacitors. This layer also protects the top mirror from the atmosphere and possible physical damages.

4.2.6 Airpost Formation

Prior to the airbridge metalization, the post openings are formed with a normal PL. Then the samples are hard baked in oven at 140 °C for 30 minutes, so that the airpost resist doesn't get dissolved in the airbridge PL. After the postbake, RIE is applied to thin the resist down to about $0.6\mu m$, so that a $0.8 - 0.9\mu m$ thick metalization will be enough to form the airbridge. Similar to wet-etching, RIE is done in several steps, controlling the etch rate and depth using DekTak profilometer. When the desired resist thickness is reached, the samples are ready for airbridge lithography.

4.2.7 Airbridge Metalization

This is the most critical step of the process. The yield of the whole process depends on the success of the airbridge formation. Especially, the lift-off of the airbridge metal is very critical. After image reversal PL development, process yields increased drastically. Therefore image reversal PL is applied in this step, followed by a $0.8 - 0.9\mu m$ thick Ti/Au metalization. The evaporated metal connects the two airposts to each other, forming a bridge that sits on top of the hard-baked and thinned post resist. This resist layer is dissolved in lift-off acetone. The bridge metal hangs on the air, defining an airbridge across the posts. The deposited metal also serves as the upper plate of the MIM capacitors.

Airbridge construction is needed to obtain low parasitic capacitances and the ability to carry higher currents. A classical interconnect metal deposited directly on the sample surface results in a higher parasitic capacitance than the airbridge connection. Therefore for high-speed photodetection, airpost formation and airbridge metalization steps are essential fabrication processes. In Figure 4.1, a microphotograph of a completed RCE Schottky photodiode is shown.

4.2.8 Fabrication Process for p-i-n Photodiodes

Except one level, the fabrication process for p-i-n photodiodes is the same as Schottky photodiodes. For p-i-n photodetectors, a p^+-ohmic contact is formed using a mask different than the Schottky mask used for Schottky photodiodes. p^+-ohmic contact is formed with a normal PL followed directly by a $0.15 - 0.2\mu m$ thick Ti/Au metalization and lift-off process. Since the p^+ layer is at the top of the wafer, no etch is needed before metalization. To create an ohmic contact, the deposited metal should be annealed by RTA. Therefore we annealed both n^+ and p^+ ohmic metals in the same RTA step (450 °C, 45 seconds). This step should be done before interconnect metalization. Once the interconnect metal is deposited onto the sample, RTA cannot be applied anymore. A fabricated RCE p-i-n photodiode is shown in Figure 4.2.
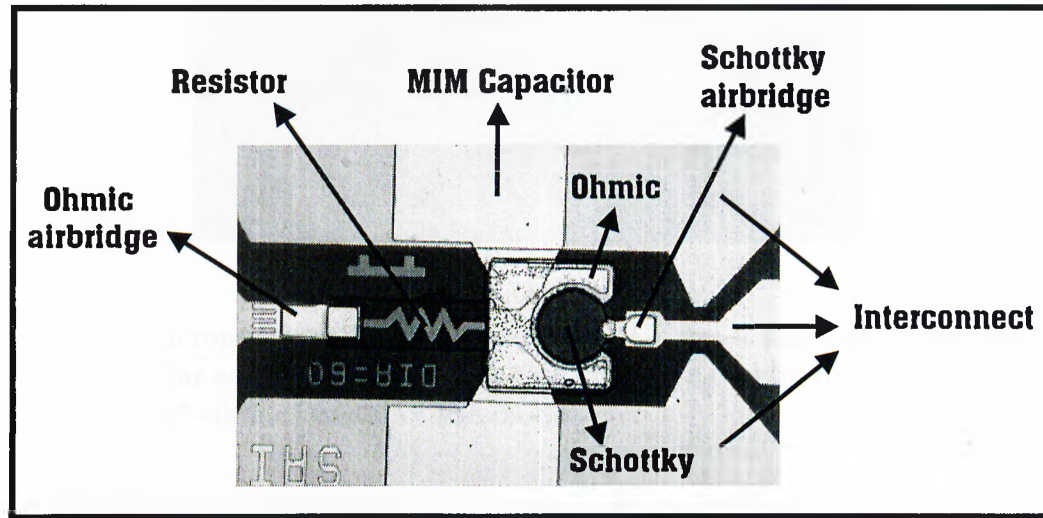
Figure 4.1: Microphotograph of a fabricated RCE Schottky photodiode with $60\mu m$ diameter circular active area. Airbridges connect the ohmic and Schottky contacts to the interconnect metal.

4.3 I-V Characterization

Current-voltage characterization is an important performance indicator for photodiodes. A good I-V characteristic promises high performance detection. I-V characterization can be done directly after the Schottky metalization or p^{+}-ohmic contact formation. It gives information about the contact (ohmic/Schottky) qualities and saves from time and extra work, if a problem has occurred in the previous process steps.

We used an HP4142B semiconductor parameter analyzer in our I-V measurements. We first checked the diode characteristic around the zero bias voltage. Once the turn-on characteristic is observed, we increased the reverse bias voltage until we reached the reverse breakdown voltage. The breakdown voltage determines the maximum reverse bias voltage that can be applied across
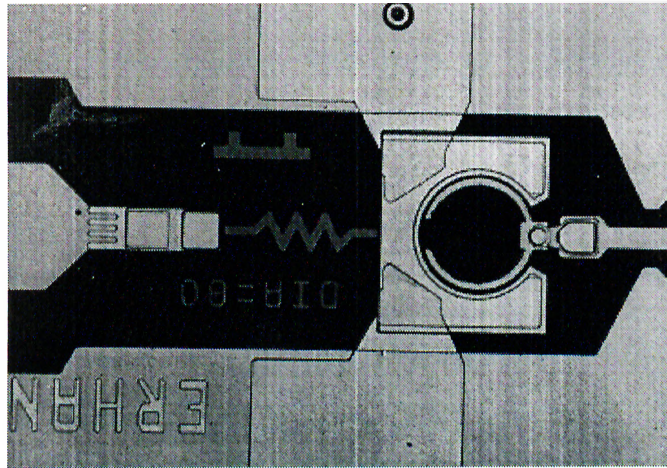
Figure 4.2: Microphotograph of a fabricated RCE p-i-n photodiode with $80\mu m$ diameter circular active area. The thin ring circumvented by the n^+-ohmic metal is the anode (p^+-ohmic) metal of the diode.

the diode during measurements. Our fabricated samples had breakdown voltages in the range of 4 - 20 Volts, depending on the design, fabrication and area of the diodes. Smaller diodes have higher breakdown voltages as shown in Figure 4.3. A 30 μm diameter circular p-i-n photodiode displayed a dark current of 20 pA at -1 V bias. In Schottky design few pA dark currents were observed for small area diodes, where as this increased up to few nA for large area devices.
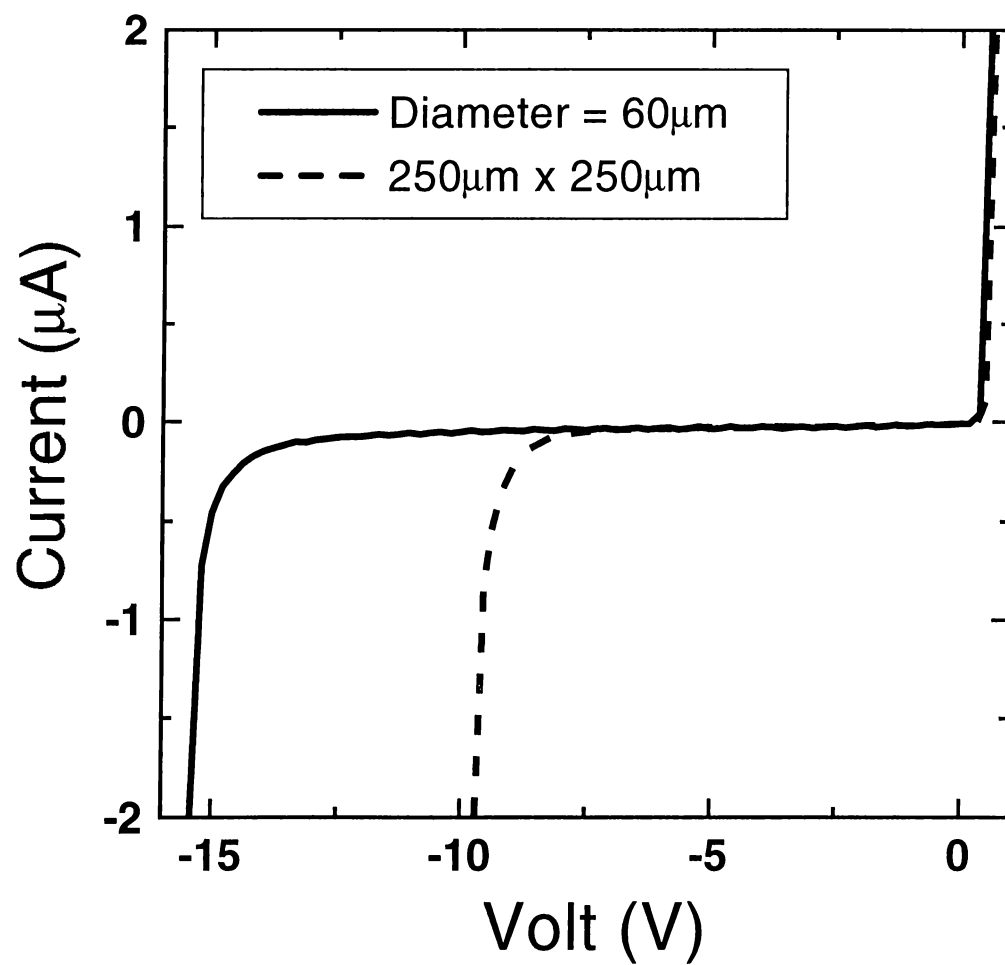
Figure 4.3: I-V measurement of two RCE p-i-n photodiodes which shows the diode area dependence of the breakdown voltage.

Chapter 5

Quantum Efficiency and Bandwidth Measurements

After a successful fabrication, quantum efficiency and bandwidth characterizations are made. These two measurement results determine the performance of a photodiode. We achieved high bandwidth-efficiency products from both Schottky and p-i-n designs. Quantum efficiency measurements were done in Bilkent University. Bandwidth characterization is performed both in Bilkent University and Boston University.

5.1 Quantum Efficiency Measurements

The quantum efficiency measurements were made with the experimental setup shown in Figure 5.1. A tungsten-halogen projection lamp is used as the light source. Computer controlled monochromator takes the light from this source and gives monochromatic light as output, which is chopped and coupled to a $62.5\mu m$ diameter multimode fiber. The monochromatic light is delivered to the devices by a lightwave fiber probe, and the electrical characterization was carried out on a probe station. Chopper output and generated photocurrent are sent to a lock-in amplifier which displays the amplitude and phase values of the output current. The incident power spectrum was measured by a calibrated optical
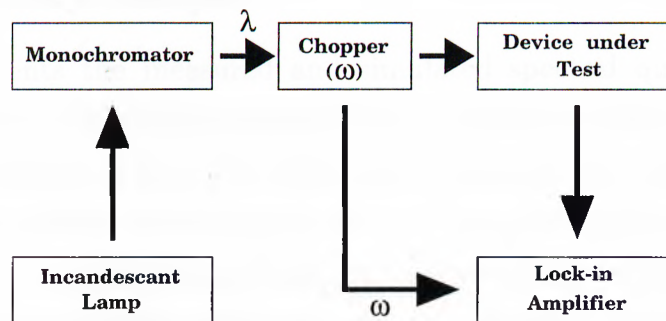
Figure 5.1: A simple diagram of the quantum efficiency measurement setup.

powermeter. We measured the devices within the spectrum of 750-900 nm, since our devices were expected to work within this spectral range.

Large area photodiodes were chosen for quantum efficiency measurements. Largest devices on our photomask have 250x250 μm active area (Figure 5.2). We obtained the best quantum efficiency results from these devices since they ensure to collect all of the light coming out from the fiber.
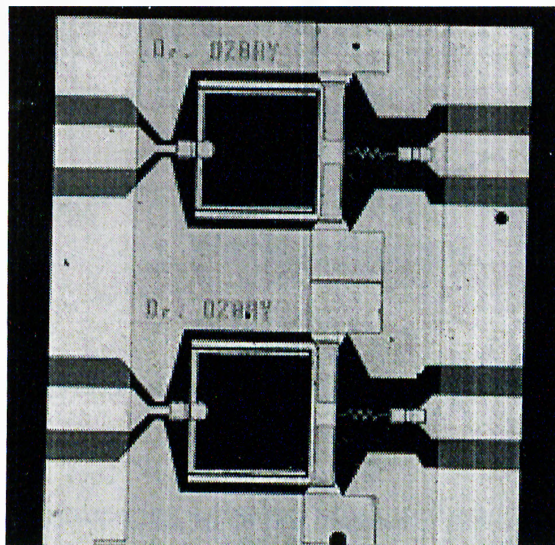

Figure 5.2: A microphotograph of two large area (250x250 μm) p-i-n photodiode which are used for quantum efficiency measurements.

5.1.1 Schottky Sample

Figure 5.3 presents the measured and simulated spectral quantum efficiency characteristics of RCE Schottky photodiode. A peak quantum efficiency of 46% at 827 nm is obtained at zero bias. Simulations indicate that a peak efficiency of 58% should be possible. Increasing the reverse bias increased the efficiency up to 50%. After 2.5 V, the photodiode begins to operate within the breakdown region, leading to carrier tunneling and avalanche multiplication. The FWHM of the measured and calculated quantum efficiency peaks are 10 and 9 nm, respectively.
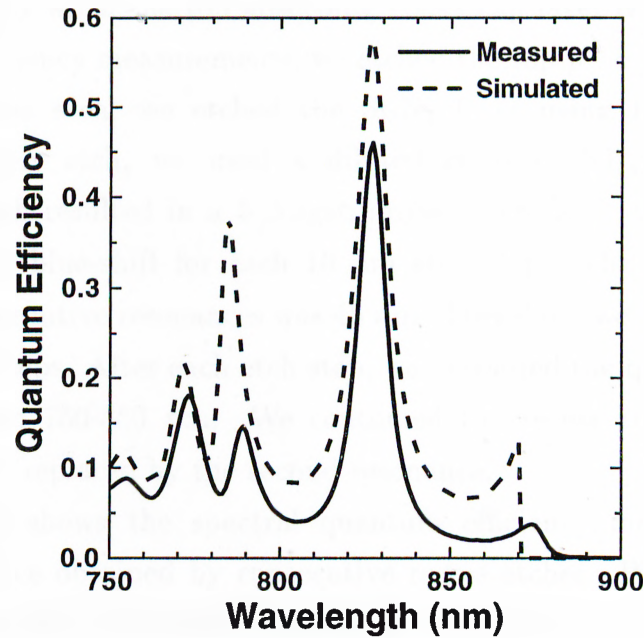
Figure 5.3: Measured and simulated quantum efficiency spectrum of RCE Schottky photodiode.

We attribute the discrepancy between measured and simulated peak efficiencies to the optical scattering losses due to surface roughness of the Schottky metal. AFM studies in Boston University have shown huge fluctuations on the thin Au layer. The broadening of the resonant peak width can be explained by the extra losses introduced within the absorbing Au top mirror. Nevertheless,

the measured $\eta = 0.46$ of the RCE structure represents an approximately five-fold improvement over the single-pass efficiency expected from the thin GaAs absorbing layer at this wavelength.

5.1.2 P-I-N Sample

As explained in Chapter 3, a major advantage of p-i-n design is its top mirror design (semiconductor-air interface), which allows us to tune the resonant wavelength after fabrication. Reflectivity measurements had shown that a 95% peak efficiency should be observable. Theoretical simulations promised near unity quantum efficiency when the top absorbing GaAs cap layer is removed. During the quantum efficiency measurements, we etched the top p^+ layer in small steps.

Prior to recess etch, we etched the Si_3N_4 layer using HF etchant. For a controlled recess etch, we used a diluted etchant ($NH_4OH:H_2O_2:H_2O = 14:2.4:2000$) which resulted in a 5 Angstrom/sec etch rate. By simulation, we expected a 4 nm blue-shift for each 10 nm etch step. The spectral distance between two consecutive resonances was 45 nm. Therefore, we etched the sample in 20-25 second steps. After each etch step, we measured the quantum efficiency spectrum between 750-850 nm. We continued the recess etch until the first resonance peak is replaced by the second resonance.

Figure 5.4(a) shows the spectral quantum efficiency measurements of a 250x250 μm device obtained by consecutive recess etches. Plot 1 corresponds to the as-grown wafer, while plots 2, 3, 4 and 5 correspond to cumulative recess etches of 25, 50, 75 and 100 nm respectively. The peak experimental quantum efficiency (88%) of the as grown sample at 816 nm, increases to $> 90\%$ values after the top absorbing GaAs layer is etched. The peak quantum efficiency remains almost constant afterwards until the resonance wavelength reaches to the lower edge of the Bragg mirror ($\sim$780 nm). When the first peak passes 800 nm, the second resonance arises around the upper edge of the Bragg mirror ($\sim$840 nm) and peak efficiency stays above 90% after 835 nm. The second resonance reaches a maximum quantum efficiency of 92% at 823 nm.
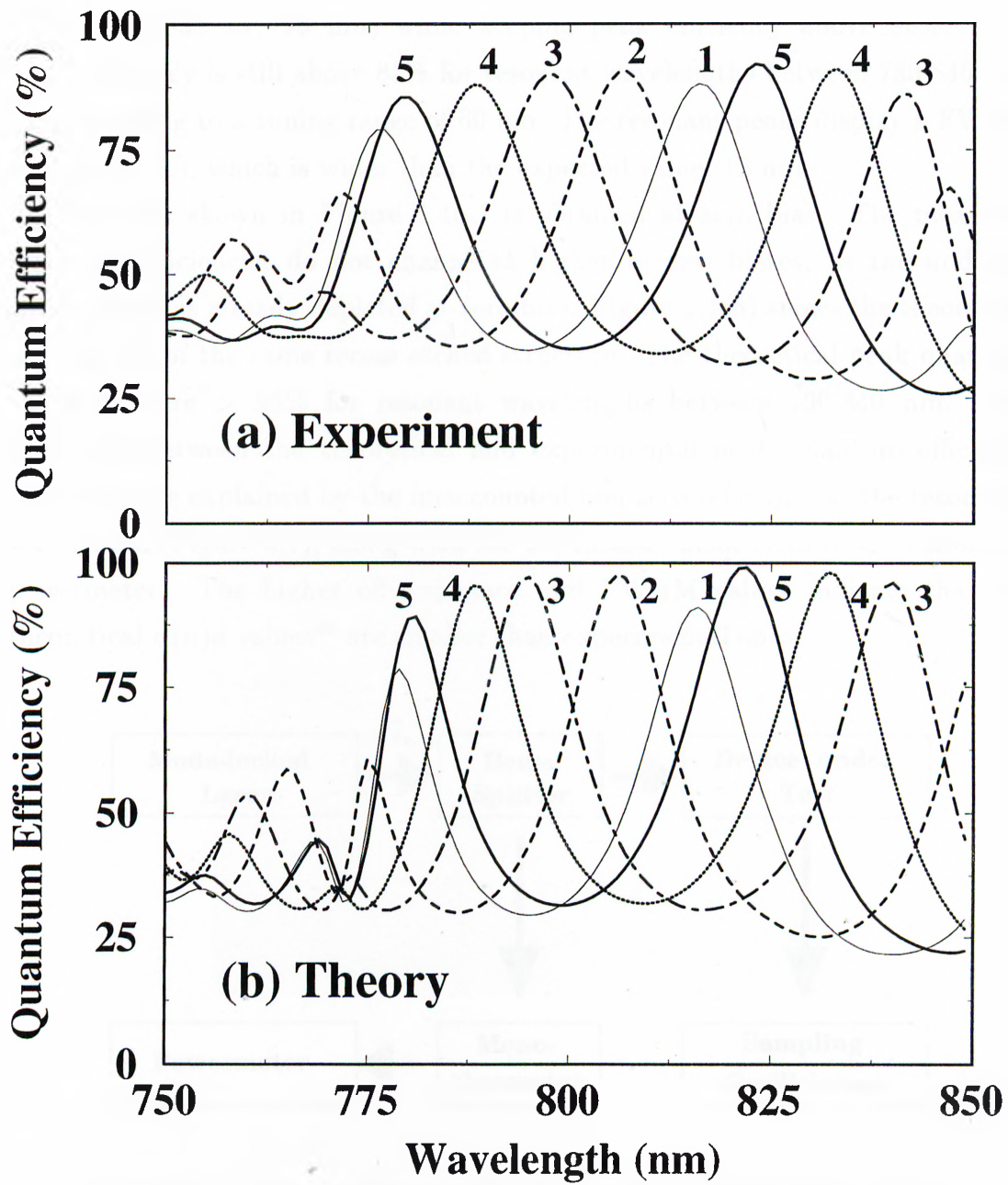
Figure 5.4: (a) Experimental and (b) theoretical photoresponse characteristics of fabricated RCE p-i-n photodiodes. Plot 1 corresponds to as-grown sample, while plots 2-5 correspond to the characteristics after consecutive recess etches.

As seen in Figure 5.4(a), the resonance wavelength can be tuned for a total of 40 nm (835 to 795 nm) while keeping peak efficiency above 90%. The peak efficiency is still above 85% for resonant wavelengths between 780-840 nm, corresponding to a tuning range of 60 nm. The resonant peaks display a FWHM around 15 nm, which is wider than the expected value, 12 nm.

The data shown in Figure 5.4(a) is obtained at zero bias. The measured quantum efficiencies do not change at higher reverse biases, as the undoped active region is already depleted at zero bias. Figure 5.4(b) shows the theoretical simulations of the same recess etched structure. The theoretical peak quantum efficiencies are > 95% for resonant wavelengths between 790-840 nm. The difference between the theoretical and experimental peak quantum efficiency values can be explained by the unaccounted non-zero reflection at the resonance wavelength (Figure 3.7), along with the 2% measurement error of the calibrated powermeter. The higher off-resonance and FWHM values indicate that the theoretical $\alpha(n)d$ values[46] are smaller than experimental ones.
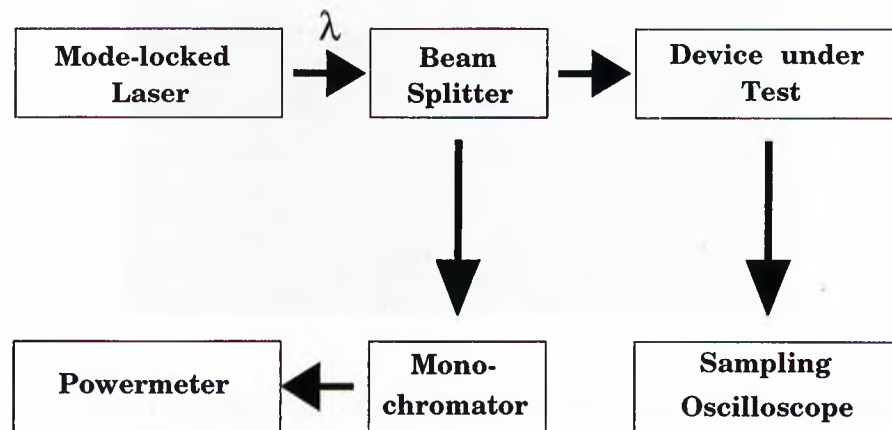

Figure 5.5: A simple diagram of the bandwidth measurement setup.

5.2 Bandwidth Measurements

High-speed measurements of Schottky samples are performed at the Photonic Research Laboratory of Boston University. Bandwidth of p-i-n photodiodes are measured both in Bilkent University and Boston University. Better results are obtained at Boston University due the faster 50 GHz scope. A schematic diagram of the measurement setup is shown in Figure 5.5. A picosecond mode locked Ti:sapphire laser tuned to resonant wavelength is used for our measurements. The optical pulses from the laser were coupled into a single-mode fiber, and the other end of the fiber was brought in close proximity of the p-i-n photodiode by means of a probe station. The temporal response of a photodiode is measured by a 50 GHz sampling scope.

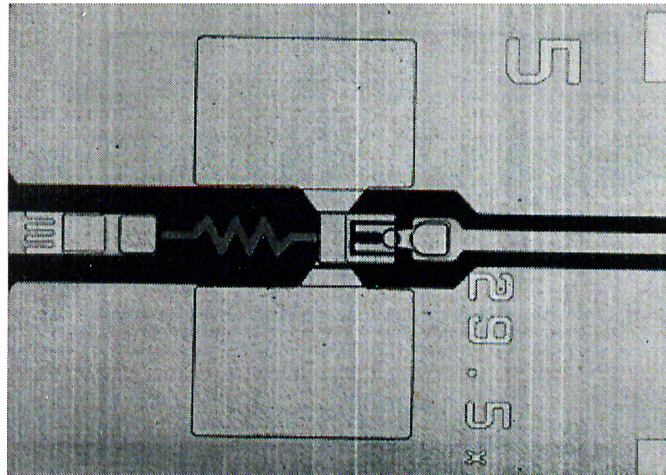Figure 5.6: A microphotograph of a fabricated small area RCE p-i-n photodiode.

As expected, the best results, i.e. fastest responses are measured from small area photodiodes. Large area photodiodes were RC-limited, whereas in small area photodiodes the operation bandwidth was limited by carrier transit times. Figure 5.6 shows fabricated RCE p-i-n photodiode with an active area of 30x12 μm.

5.2.1 Schottky Sample

Figure 5.7 shows the temporal response of a small area (8x14 μm) RCE Schottky photodiode. The best measured FWHM is 12 psec under 8 V reverse bias. Consedering a 9 psec FWHM for the 50 GHz scope, the FWHM of the detector is estimated to be less than 8 psec. Theoretically expected 3-dB bandwidth is 78 GHz. The detector response becomes considerably slower for reverse biases lower than 6 V. This observation indicates that a 6 V reverse bias is needed for full depletion of the absorbing GaAs layer, which is a result of the relatively high-doping in the depletion region. Hence, our Schottky photodiodes display high-speed performance only at relatively large reverse bias.
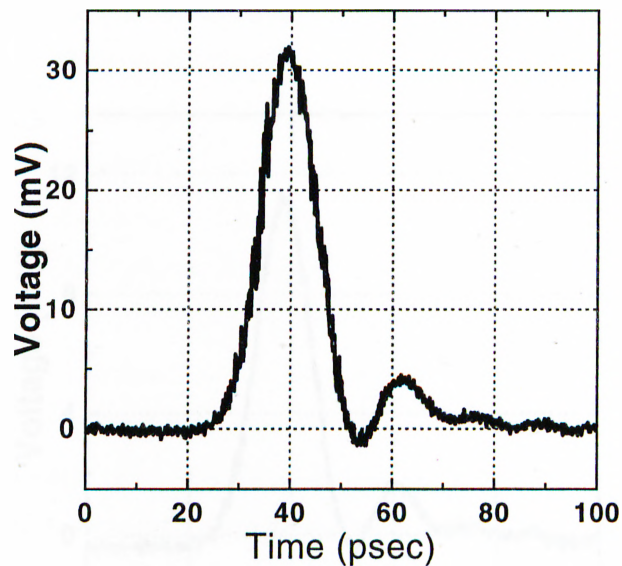

Figure 5.7: Pulse response of a 8x14 μm RCE Schottky photodiode.

5.2.2   P-I-N Sample

The best high-speed result of our p-i-n sample is obtained with a 7x13 μm photodiode. The temporal response is presented in Figure 5.8. The measured photodiode output has a 12 psec FWHM. The Fourier transform of the data has a 3-dB bandwidth of 38 GHz. As in Schottky sample, we were limited by the scope in this measurement. When the measured data is corrected by deconcolving the scope response, the actual bandwidth corresponds to 50 GHz. The RC time constant of our device is 1.2 psec, corresponding to a 3-dB bandwidth of 230 GHz. The response of the device is mostly limited by the hole (7.5 psec) and electron (4.5 psec) transit times. Using these numerical values, we predict a 3-dB bandwidth of 50 GHz for the device under test, in good agreement with the deconvolved high-speed measurements.
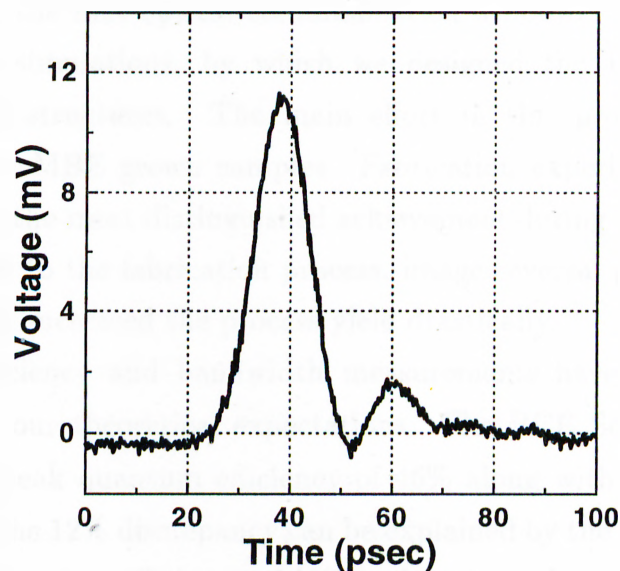

Figure 5.8: Pulse response of a 7x13 μm RCE p-i-n photodiode.

Chapter 6

Achievements and Future Directions

In the foregoing chapters we presented our work on design, fabrication and characterization of high performance GaAs/AlGaAs based RCE photodiodes operating within the first optical communication window. We began our work with theoretical simulations, by which we designed the RCE Schottky and p-i-n photodiode structures. The main effort in this project is devoted to the fabrication of MBE grown samples. Fabrication experience in clean-room environment was the most distinguished achievement during this two-year work. As a contribution to the fabrication process, image reversal photolithography is introduced, which increased the process yield drastically.

Quantum efficiency and bandwidth measurements have shown reasonable agreements with our theoretical expectations. The RCE Schottky photodiode demonstrated a peak quantum efficiency of 46% along with a 12 psec FWHM pulse response. The 12% discrepancy can be explained by the non-perfect top Au mirror. A peak quantum efficiency of 92% and again a 12 psec FWHM temporal response is displayed by the RCE p-i-n photodiode. The unaccounted non-zero reflection at resonance wavelength prevented us to reach peak efficiencies beyond 95%. Pulse responses of both Schottky and p-i-n samples were experimental setup limited. When the scope response is deconvolved, maximum 3-dB bandwidth

of 78 and 50 GHz is obtained for Schottky and p-i-n samples respectively. These measurements result in high bandwidth-efficiency products: 36 GHz for Schottky sample and 46 GHz for p-i-n sample. Both products indicate the best performance demonstrated for Schottky and p-i-n type RCE photodiodes in scientific literature.

Useful results can be deduced from a comparison between the performances of RCE Schottky and p-i-n photodiodes. From the efficiency point of view, p-i-n designs are preferable. Schottky photodiodes suffer from the absorbing Schottky metal, which also acts as the top mirror of the cavity. This is not the case in p-i-n photodiode, where the top mirror is the semiconductor-air interface. This feature of p-i-n design allows to tune the resonant wavelength by recess etching after fabrication. Schottky design is not tunable after fabrication due the top mirror. Although the deconvolved bandwidths show that the Schottky sample is faster than the p-i-n sample, this is mainly due to its thinner absorbing layer. An equivalent thin absorbing layer in a heterojunction RCE p-i-n photodiode with a higher reflectivity top mirror should perform higher bandwidths. Performance of the RCE Schottky photodiode can be increased if the problems with the top mirror is solved. Introduction of a transparent indium-tin-oxide (ITO) film (instead of Au) may solve this problem,[51,52] which is among our near future plans.

Further development of RCE photodiodes operating in the 800-850 nm wavelength regime will be continued. Over 100 GHz bandwidth is the next target with a thinner active region p-i-n design. To obtain still high quantum efficiencies, such a design needs a higher reflectivity top mirror. A dielectric (SiO_2/Si_3N_4) Bragg reflector is planned to be utilized as top mirror.

The main effort will be devoted to the development of RCE photodiodes operating at 1.3 μm and 1.55 μm, where most of the optical fiber communication takes place. High performance RCE photodiodes are promising detectors for high bit-rate optical communication systems. Their wavelength selectivity can be used for WDM applications in these systems. The theoretical work is completed for several designs working at these wavelengths. We will develop the fabrication process for several long-wavelength material systems (InP/InGaAs/InAlAs,

InAs/InSb, low temperature-grown (LT) GaAs). The measurement setups will also be developed both for quantum efficiency measurement in the long-wavelength regime and higher bandwidth measurements. Electro-optic sampling, photoconductive sampling, and two-laser beating measurements are the high-speed measurement techniques we are considering for > 100 GHz bandwidths. Following our successful results at $\lambda = 0.85\ \mu m$ window, we hope to achieve world-record detector performance in the $\lambda = 1.3\ \mu m$ and $\lambda = 1.55\ \mu m$ wavelength regimes.

Bibliography

[1] E.Bowers and Y.G.Wey, Handbook of Optics, chap.17, McGraw-Hill, New York, 1996.

[2] S. Y. Wang, and D. M. Bloom, 100 GHz bandwidth planar GaAs Schottky photodiode, Electron. Lett. **19**, 554 (1983).

[3] D. G. Parker, P. G. Say, A. M. Hanson, and W. Sibbett, 110 GHz high efficiency photodiodes fabricated from indium tin oxide/GaAs, Electron. Lett. **23**, 527 (1987).

[4] E. Ozbay, K. D. Li, and D. M. Bloom, 2.0 psec GaAs monolithic photodetector and all electronic sampler, IEEE Photonics Technol. Lett. **3**, 570 (1991).

[5] K. D. Li, E. Ozbay, and D. M. Bloom, 1.8 psec, 200 GHz GaAs photodiode and all-electronic sampler, Proceedings of Conference on Lasers and Electro Optics (CLEO), May 1991.

[6] Y. G. Wey, K. S. Giboney, J. E. Bowers, M. J. Rodwell, P. Silvistre, P. Thiagarajan, and G. Y. Robinson, 110 GHz GaInAs/InP p-i-n Photodiodes with Integrated Bias Tees and Matched Resistors, IEEE Photonics Technol. Lett. **5**, 1310 (1993).

[7] Y. G. Wey, M. Kagewa, A. Mar, K. J. Williams, K. Giboney, D. L. Crawford, J. E. Bowers, and M. J. Rodwell, Hybrid Integration of an InGaAs/InP p-i-n Photodiode with an Ultrafast Sampling Circuit, IEEE J. Lightwave Technol. **5**, 1310 (1993).

[8] S. Gupta, J. F. Whitaker, S. L. Williamson, G. A. Mourou, L. Lester, K. C. Hwang, P. Ho, J. Mazurowski, and J. M. Ballingall, High-Speed Photodetector Applications of GaAs and InGaAs/GaAs Grown by Low-Temperature Molecular Beam Epitaxy, J. Electron. Materials. **22**, 1449 (1993).

[9] P. Kordos, A. Forster, M. Marso, and F. Ruders, 550 GHz bandwidth photodetector on low-temperature grown molecular-beam epitaxial GaAs, Electron. Lett. **34**, 119 (1998).

[10] K. Kishino, M. S. Unlu, J. I. Chyi, J. Reed, L. Arsenault, and H. Morkoc, Resonant cavity-enhanced (RCE) photodetectors, IEEE J. Quantum Electron. **27**, 2025 (1991).

[11] M. S. Unlu and S. Strite, Resonant cavity enhanced photonic devices, J. Appl. Phys. Rev. **78**, 607 (1995).

[12] S. Y. Hu, J. Ko, and L. A. Coldren, Resonant-cavity InGaAs/InAlGaAs/InP photodetector arrays for wavelength demultiplexing applications, Appl. Phys. Lett. **70**, 2347 (1997).

[13] S. Y. Hu, J. Ko, and L. A. Coldren, 1.55 μm pie-shaped resonant-cavity photodetector arrays for direct-coupled wavelength demultiplexing applications, Electron. Lett. **33**, 1486 (1997).

[14] J. Sarathy, K. A. Anselm, B. G. Streetman, and J. C. Campbell, Narrow linewidth, tunable distributed feedback photodetector, Appl. Phys. Lett. **69**, 3123 (1996).

[15] B. M. Onat, M. Gokkavas, E. Ozbay, E. P. Ata, E. Towe, and M. S. Unlu, 100-GHz Resonant Cavity Enhanced Schottky Photodiodes, IEEE Photonics Technol. Lett. **10**, 707 (1998).

[16] M. S. Unlu, M. Gokkavas, B. M. Onat, E. Ata, E. Ozbay, R. P. Mirin, K. J. Knopp, K. A. Bertness, and D. H. Christensen, High bandwidth-efficiency

resonant cavity enhanced Schottky photodiodes for 800-850 nm wavelength operation , Appl. Phys. Lett. **72**, 2727 (1998).

[17] M. S. Unlu, Y. Leblebici, S. M. Kang, and H. Morkoc, Transient Simulation of Resonant Cavity Enhanced Heterojunction Photodiodes, IEEE Photonics Technol. Lett. **4**, 1366 (1992).

[18] M. S. Unlu, B. M. Onat, and Y. Leblebici, Transient Simulation of Heterojunction Photodiodes-Part II: Analysis of Resonant Cavity Enhanced Photodetectors, IEEE J. Lightwave Technol. **13**, 406 (1995).

[19] Hsin-Han Tung and Chien-Ping Lee, Design of a Resonant-Cavity-Enhanced Photodetector for High-Speed Applications, IEEE J. Quantum Electron. **33**, 753 (1997).

[20] C. C. Barron, C. J. Mahon, B. J. Thibeault, G. Wang, W. Jiang, L. A. Coldren, and J. E. Bowers Resonant-cavity-enhanced pin photodetector with 17 GHz bandwidth-efficiency product, Electron. Lett. **30**, 1796 (1994).

[21] H. Nie, K. A. Anselm, C. Lenox, P. Yuan, C. Hu, G. Kinsey, B. G. Streetman, and J. C. Campbell, Resonant-Cavity Seperate Absorption, Charge and Multiplication Avalanche Photodiodes with High-Speed and High Gain-Bandwidth Product, IEEE Photonics Technol. Lett. **10**, 409 (1998).

[22] S. S. Jha, Perspectives in Optoelectronics, chap.6, World Scientific Publishing, Singapore, 1995.

[23] B. L. Sharma, Metal-Semiconductor Schottky Barrier Junctions and Their Applications, chap.1, Plenum Press, New York, 1984.

[24] E. Ozbay, Breaking world records in high speed microelectronics, Stanford University Ph.D. thesis, February 1992.

[25] S. M. Sze, Physics of Semiconductor Devices, Wiley, New York, 1981.

[26] M. S. Unlu, K. Kishino, J. I. Chyi, L. Arsenault, J. Reed, S. N. Mohammad, and H. Morkoc, Resonant cavity enhanced AlGaAs/GaAs heterojunction photo-transistors with an intermediate InGaAs layer in the collector, Appl. Phys. Lett. **57**, 750 (1990).

[27] E. Ozbay, M. S. Islam, B. Onat, M. Gokkavas, O. Aytur, G. Tuttle, E. Towe, R. H. Henderson, and M. S. Unlu, Fabrication of High-Speed Resonant Cavity Enhanced Schottky Photodiodes, IEEE Photonics Technol. Lett. **9**, 672 (1997).

[28] E. P. Ata, N. Biyikli, E. Demirel, E. Ozbay, M. Gokkavas, B. Onat, M. S. Unlu, G. Tuttle, High-speed resonant-cavity-enhanced Schottky photodiodes, Proceedings of Conference on Lasers and Electro Optics (CLEO), May 1998.

[29] B. Corbett, L. Considine, S. Walsh, and W. M. Kelly, Narrow bandwidth long wavelength resonant cavity photodiodes, Electron. Lett. **29**, 2148 (1993).

[30] A. Srinivasan, S. Murtaza, J. C. Campbell, and B. G. Streetman, High quantum efficiency dual wavelength resonant-cavity photodetector, Appl. Phys. Lett. **66**, 535 (1995).

[31] K. A. Anselm, S. S. Murtaza, C. Hu, H. Nie, B. G. Streetman, and J. C. Campbell, A Resonant-Cavity, Seperate-Absorption-and Multiplication, Avalanche Photodiode with Low Excess Noise Factor, IEEE Electron Device Lett. **17**, 91 (1996).

[32] H. Nie, K. A. Anselm, C. Hu, S. S. Murtaza, B. G. Streetman, and J. C. Campbell, High-speed resonant-cavity seperate absorption and multiplication avalanche photodiodes with 130 GHz gain-bandwidth product, Appl. Phys. Lett. **70**, 161 (1997).

[33] C. Yeh, Handbook of Fiber Optics: Theory and Application, Academic Press, London, 1989.

[34] S. S. Murtaza, K. A. Anselm, A. Srinivasan, B. G. Streetman, J. C. Campbell, J. C. Bean, and L. Peticolas, High-Reflectivity Bragg Mirrors for Optoelectronic Applications, IEEE J. Quantum Electron. **31**, 1819 (1995).

[35] F. Y. Huang, A. Salvador, X. Gui, N. Teraguchi, and H. Morkoc, Resonant-cavity GaAs/InGaAs/AlAs photodiodes with a periodic absorber structure, Appl. Phys. Lett. **63**, 141 (1993).

[36] I-H. Tan, J. J. Dudley, D. I. Babic, D. A. Cohen, B. D. Young, E. L. Hu, J. E. Bpwers, B. I. Miller, U. Koren, and M. G. Young High Quantum Efficiency and Narrow Absorption Bandwidth of the Wafer-Fused Resonant $In_{0.53}Ga_{0.47}As$ Photodetectors, IEEE Photonics Technol. Lett. **6**, 811 (1994).

[37] S. S. Murtaza, I-H. Tan, R. V. Chelakara, M. R. Islam, A. Srinivasan, K. A. Anselm, J. E. Bowers, E. L. Hu, R. D. Dupuis, B. G. Streetman, and J. C. Campbell, High-Efficiency, Dual Wavelength, Wafer-Fused Resonant-Cavity Photodetector Operating at Long Wavelengths, IEEE Photonics Technol. Lett. **37**, 679 (1995).

[38] M. S. Unlu, K. Kishino, H. J. Liaw, and H. Morkoc A theoretical study of resonant cavity-enhanced photodetectors with Ge and Si active regions, J. Appl. Phys.. **71**, 4049 (1992).

[39] S. S. Murtaza, H. Nie, J. C. Campbell, and L. J. Peticolas, Short-Wavelength, High-Speed Resonant-Cavity Photodetector, IEEE Photonics Technol. Lett. **8**, 927 (1996).

[40] M. Seto, W. B. de Boer, V. S. Sinnis, A. P. Morrison, W. Hoekstra, and S. de Jager, Si/SiGe resonant-cavity photodiodes for optical storage applications, Appl. Phys. Lett. **72**, 1550 (1998).

[41] A. G. Dentai, R. Kuchibhotla, J. C. Campbell, C. Tsai, and C. Lei, High quantum efficiency, long wavelength InP/InGaAs microcavity photodiode, Electron. Lett. **27**, 2125 (1991).

[42] K. Xie, J. H. Zhao, Y. Shi, H. Lee, and G. Olsen,Resonant Cavity Enhanced GaInAsSb-AlAsSb Photodetector Grown by MBE for Mid-IR Applications, IEEE Photonics Technol. Lett. **8**, 667 (1996).

[43] M. H. MacDougal and P. D. Dapkus, Wavelength Shift of Selectively Oxidized Al_xO_y-AlGaAs-GaAs Distributed Bragg Reflectors, IEEE Photonics Technol. Lett. **9**, 884 (1997).

[44] M. Gokkavas, Design and characterization of resonant cavity enhanced Schottky photodiodes, Bilkent University M.S. thesis, September 1996.

[45] Y-C. Tzeng, S. S. Li, and P. Ho, A GaAs-Schottky Barrier Photodiode with High Quantum Efficiency-Bandwidth Product by Using a Multilayer Reflector, IEEE Trans. Electron. Devices **40**, 348 (1993).

[46] E. D. Palik, Handbook of Optical Constants of Solids, Academic Press, Orlando, 1985.

[47] S. S. Murtaza, I.-H. Tan, J. E. Bowers, E. L. Hu, K. A. Anselm, M. R. Islam, R. V. Chelakara, R. D. Dupuis, B. G. Streetman, and J. C. Campbell, High-Finesse Resonant-Cavity Photodetectors with an Adjustable Resonance Frequency, IEEE J. Lightwave Technol. **14**, 1081 (1996).

[48] M. S. Islam, Fabrication and characterization of high-speed resonant cavity enhanced Schottky photodiodes, Bilkent University M.S. thesis, September 1996.

[49] E. P. Ata, Fabrication and characterization of high-speed, high quantum efficiency, resonant cavity enhanced Schottky photodiodes, Bilkent University Ph.D. thesis, July 1998.

[50] M. Spak, D. Mammato, S. Jain, and D. Durham, Mechanism and Lithographic Evaluation of Image Reversal in AZ 5214 Photoresist, presented at Seventh International Technical Conference on Photopolymers, Ellenville, New York.

[51] W. Gao, P. R. Berger, R. G. Hunsperger, G. Zydzik, W. W. Rhodes, H. M. O;Bryan, D. Sivco, and A. Y. Cho, Transparent and opaque Schottky contacts on undoped InAlAs grown by molecular beam epitaxy, Appl. Phys. Lett. **66**, 3471 (1995).

[52] W. A. Wohlmuth, J.-W. Seo, P. Fay, C. Caneau, and I. Adesida, A High-Speed ITO-InAlAs-InGaAs Schottky-Barrier Photodetector, IEEE Photonics Technol. Lett. **9**, 1388 (1997).